University of Alberta

Integration of Nanomechanical Resonators in Microfluidic Systems for Specific Protein Detection

by

Wooree Ko

A thesis submitted to the Faculty of Graduate Studies and Research
in partial fulfillment of the requirements for the degree of

Masters of Science

in

Micro-Electro-Mechanical-Systems (MEMS) and Nanosystems

Department of Electrical and Computer Engineernig

Fall 2009

Edmonton, Alberta

Examining Committee

Chris Backhouse, Electrical and Computer Engineering

Stephane Evoy, Electrical and Computer Engineering

Duncan Elliott, Electrical Engineering

Lorenz Sigurdson, Mechanical Engineering

Abstract

Nanomechanical resonators offer a pathway towards highly sensitive and label-free detection of biomolecules by transducing the mass of bound analytes into resonant frequency shifts. Zeptogram level and even single cell detections have been successfully achieved by others. However, these experiments have been performed through traditional “dip-and-dry” method, requiring the use of a large quantity of analyte. Such a system is not readily amenable to automation, is subject to contamination and is prone to inter-run variation. Integration of nanomechanical resonators into a microfluidic system would facilitate sample delivery and provide a stable Lab-On-a-Chip (LOC) system that could be effectively used for diagnostic tests. There have been a few demonstrations of integrating nanomechanical resonators with microfuidic systems. However, these works involved external syringe pumps and valves for sample delivery which make their system bulky, complex and not suitable for point-of-care testing applications. Here we have developed a nanomechanical resonator-based microfluidic system that delivers sample using on-chip automated pump and valve systems and that demonstrates the biosensing capabilities with the limit of detection in femtogram range using minute amount of sample. To our best of

knowledge, this is the first integration of nanoresonator-based sensing platform with the automated on-chip sample delivery system. Such integration can provide the system with simplicity, portability and potential realization as easily accessible point-of-care diagnostic tools.

Nanoresonator arrays operating at 4.8 MHz ~ 10 MHz were fabricated and their surfaces were modified with vapour-deposited mercaptopropyl trimethoxysilane (MTPMS) to sequentially immobilize biotin (0.6 mg/mL) and streptavidin protein (1 mg/mL and 10 μm/mL). Based on resonance assaying, the calculated mass-per-area for the bound streptavidin were 1.23 mg/m^2 for 1 mg/mL and 1.01 mg/m^2 for 10 μm/mL streptavidin concentrations. These values correspond to one streptavidin per 80 $(nm)^2$ and 95 $(nm)^2$ or 81 % and 63 % coverage over the biotin-covered surface, respectively. The overall lowest detected mass from the resonators was 8.8 fg of biotin.

Acknowledgement

I would like to thank my supervisors, Dr. Chris Backhouse and Dr. Stephane Evoy, for giving me a great opportunity to work on such a fascinating project with great people and in the world-class facilities. I also thank all the past and present staff and fellow students in NEMS Lab and AML for sharing their knowledge and for being good friends in the past two years. Special thanks to Dr. Miro Belov for his assistance with inteferometry setup, Dr. Vince Wright for helping me with silanization, Govind Kaigala for electronics, Aruna Kroetch and Lee Fischer for sharing their fabrication expertise, Dr. Dammika Manage and Dr. Wanho Song for their support and guidance throughout the years in the graduate studies.

I would like to acknowledge past and present Nanofab staff for training me and maintaining the equipment I constantly used. Also, I thank Nanofab users who were willing to share their knowledge and experiences.

Lastly, I would like to thank my family and friends for their endless love, support and prayers.

Table of Contents

List of Tables

List of Figures

List of Abbreviations

AFM	Atomic force microscopy
AML	Applied miniaturisation laboratory
BOE	Buffered oxide etch
CVD	Chemical vapour deposition
DI	Deionized
DMSO	Dimethyl sulfoxide
EBL	Electron beam lithography
ELISA	Enzyme linked immunosorbent assay
FWH	Full width half maximum
KOH	Potassium hydroxide
LOC	Lab on a chip
MPTM	Mercaptopropyl trimethoxysilane
MEMS	Microelectromechanical systems
µTAS	Micro total analysis system
NEMS	Nanoelectromechanical systems
PBS	Phosphate buffered solution
PDMS	Polydimethylsiloxane

PMMA	Polymethyl methacrylate
PSA	Prostate specific antigen
PZT	Lead zirconate titanate
Q	Quality factor
QCM	Quartz crystal microbalance
RIE	Reactive ion etch
SAM	Self assembled monolayer
SEM	Scanning electron microscope
SOI	Silicon on insulator
SPR	Surface plasmon resonance

Chapter 1

Introduction

Development of sensitive, reliable, rapid, portable and inexpensive biosensors has been a subject of extensive research to improve global healthcare. According to the statistics of the World Health Organization, the dominant burden of diseases are non-communicable diseases such as cardiovascular disease, cancer and respiratory disease in developed countries and infectious diseases such as HIV/AIDS, malaria and tuberculosis in developing countries [4]. A wide range of such diseases is accompanied by changes in protein concentrations in the patient's physiological fluids [5]. Detection and quantification of these protein markers are routinely carried out through immunoassays making use of the specificity and sensitivity of the antibody-antigen interaction. The biosensors designed for immunoassays can be adopted as frequent point-of-care test tools for physicians' and home use. Consequently, such use permits early and accurate

diagnosis of diseases and, thus, prompt and proper treatment of patients [6]. In addition, those biosensors can greatly benefit developing countries or remote locations with inadequately trained technicians, low-resource settings and limited resources to maintain complex equipment and handle fragile reagents. Readily usable biosensors can ultimately limit the spread of disease in the population through rapid and early detection. Development of such biosensors can revolutionize healthcare by promoting the decentralization of medical laboratory testing, thereby giving an equal opportunity of health to the public.

Since the introduction of micro-total-analysis system (μTAS), or Lab-On-a-Chip (LOC) systems by Manz in 1990s [7], the efforts to develop such biosensors have been accelerated. Lab-on-a-chip systems rely on microfluidic systems in which material is transported within micrometer scale channels. Their goal is to fully incorporate analytical procedures into flowing systems through the integration of the full functionalities of a room-sized laboratory onto a small chip. The advantages of such integration include reduced reagent and power consumption, shortened analysis time and increased detection sensitivity due to the high surface-to-volume ratio, ease of automation and reduced unit cost [8]. Development of integrated microfluidic devices is growing not only with immunoassays [9, 10] but also with DNA analysis [11] and cytometry [12].

Conventional microfluidic immunoassays involve chemically labelling proteins, typically with radioactive species, fluorescent markers or enzymes to transduce the presence of the analyte into a measurable signal [13]. Although label-based detection has been well established and widely used in microfluidic devices, the technology is not ideal due to the problems with conjugation, relatively low sensitivity and additional cost and time for labeling the biomolecules.

Microsensor platforms such as surface plasmon resonance (SPR), quartz crystal microbalances (QCMs) and micro-/nano-cantilevers have been gaining attention as alternative label-free transduction platforms. Surface plasmon resonance is an

optical measurement technique that monitors changes of refractive index induced by binding events on functionalized noble-metal surfaces. A quartz crystal microbalance detects adsorbed mass by measuring changes in mechanical resonance properties of a thin film deposited on a metal electrode. These two techniques have been widely employed in biosensing applications. However, their resolutions are relatively low such that it is difficult to detect low molecular weight molecules and low concentration samples. Most SPR systems offer resolution on the order of 100~1,000 pg/cm^2 [14] and QCMs have demonstrated sensitivities on the order of 1 ng/cm^2 in fluid [13].

Micro-/nano-resonant cantilevers are another promising platform for label-free detection of molecular systems. Zeptogram level [15] and single cell detections [16] have been successfully achieved. However, these demonstrated detections have been generally performed through "dip-and-dry" methods, requiring the usage of large quantities of analyte. Such an approach is not readily amenable to automation, subject to contamination, prone to inter-run variability and limits the diagnostic capability of the device. Integration of nanoresonators into a microfluidic system would facilitate sample delivery and provides a stable Lab-On-a-Chip (LOC) system that could be used routinely for diagnostic tests. Recently, Hwang *et al.* [17] detected prostate-specific-antigen (PSA) placed in a microfluidic cell with sensitivity of 0.2 ng/mL. More recently, Aubin *et al.* [18] showed the feasibility of integrating nanoresonators in microfluidic channel but actual experiments of specific detection have not been reported. Both works involved external syringe pumps for fluid handling which make the systems bulky.

We have developed a microchip that encapsulates nanoresonators, handles the sample through automated on-chip micro-pneumatic pumps and valves, and perform the specific detection of biological agents. Chapter 2 presents a literature review on micro-/nano-cantilever and microfluidic immunoassay. Chapter 3 covers the design, fabrication of the microchip and discusses the

feasibility of the resonators in the system to perform as biological sensors. Chapter 4 studies the resonator performance at various pressure levels as well as its dependency on resonance actuation mechanisms, and Chapter 5 demonstrates the biosensing capabilities of the developed system using a biotin-streptavidin complex for the proof-of-concept. A project summary and suggested future works are finally presented in Chapter 6.

Chapter 2

Literature Review

2.1. Micro-/Nano-Cantilevers

Micro-/nano-cantilevers are typically micro-/nano-meter scale “diving boards” anchored at one end to a relatively large mass [19]. These devices can be mass-fabricated from silicon using conventional micromachining techniques originally developed in the microelectronics industry. These sensors are derived from the microfabricated cantilevers used in atomic force microscopy (AFM). In AFM, a cantilever with an integrated sharp tip is used to characterize surface topography by measuring changes of its deflection or resonant frequency [13]. Cantilevers can also perform as stand-alone sensors by using the same physical principles employed in AFM. They operate in either deflection mode or resonant mode, and transduce the recognition of the molecules of interest into mechanical motions.

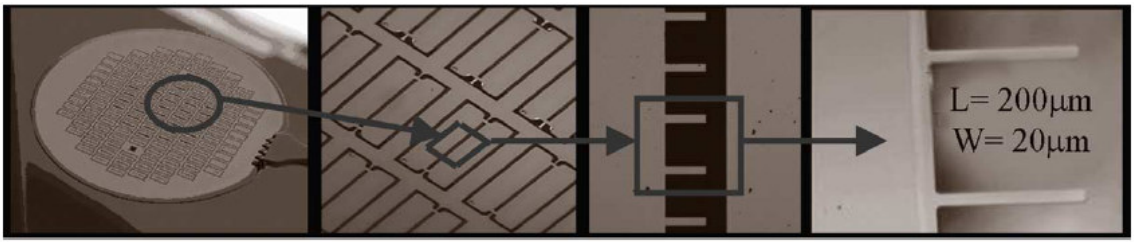

Figure 2.1: Examples of microfabricated silicon cantilevers. Reprinted with permission from ref. [1]. Copyright Elsevier, 2006

Cantilever-based devices have been demonstrated a highly sensitive label-free sensors in chemical and biological applications. More details in sensor operation and applications are presented in the following sections.

2.1.1 Deflection-based Cantilever Sensors

2.1.1.1 Principles of Operation

Static deflection of a cantilever occurs when a species adsorbed on a functionalized surface causes differential surface stresses on the opposite non-functionalized surface. The degree of cantilever deflection is measured to determine the amount of material adsorbed onto its surfaces [19]. In case of a typical rectangular cantilever beam, fixed at one end and free to move at the other end, the relationship between the differential surface stress, $\Delta\sigma$ ($\Delta\sigma_{adsorbed} - \Delta\sigma_{passivated}$), and the resulting cantilever tip displacement, Δz, approximately follows Stoney's equation [20]

$$\Delta z = \frac{3L^2(1-v)}{Et^2}\Delta\sigma \qquad (2.1)$$

where *v, E, t* and *L* are Poisson ratio, Young's modulus, the thickness and length

of the cantilever, respectively. These deflections are commonly measured through an optical reflection technique whereby a laser is focused on the cantilever and reflected onto a position sensitive detector. The varying detector signal due to motion of the reflected laser beam corresponds to the degree of cantilever deflection [13, 19, 21].

2.1.1.2 Applications

Deflection-based cantilevers have been demonstrated as sensitive detectors of chemical [22-30] and biological species [13, 31-38]. Baller *et al.* [30] developed a cantilever-array based artificial nose and detected alcohols, solvents and natural flavours in the gas phase. Thiol(-SH)-based self-assembled monolayers on gold-coated cantilevers have been used to detect toluene, water vapour [24] and explosive vapour such as trinitrotoluene (TNT) with a sensitivity of 120 parts-per-trillion (ppt) [25]. Quantization of various metal ion concentrations such as mercury [26], Cr^{2+}, Ca^{2+} and CrO_4^{2-} [27-29] has also been demonstrated. In addition, pH measurement was demonstrated using polymer coated cantilevers [22, 23].

Deflection-based cantilever sensors have also demonstrated high sensitivity in biosensing applications. Arrays of microcantilevers have been used in the field of genomics to detect a single-base mismatch in 12-nucleotide complementary DNA strands [31, 32] by generating a differential surface stress onto the functionalized cantilever surface upon target recognition. Also, the detection of Taq DNA polymerase has been demonstrated using two adjacent cantilevers, one that is functionalized with aptamers that bind specifically to Taq DNA polymerase while the other is surface-modified with single stranded DNA to act as a reference for direct detection of the differential bending [33]. Detection of bacteria such as Salmonella [34] and Bacillus subtilis [35] has also been demonstrated in liquid. In immunoassays, Arntz *et al*. [36] showed detection of

cardiac biomarker proteins, creatine kinase and myoglobin, with a detection limit below 20 μg/mL using the corresponding antibody-functionalized cantilevers. Wee *et al.* [37] and Wu *et al.* [38] have shown detection of prostate-specific antigen (PSA) at concentrations as low as 0.2 ng/mL [38]. PSA is a particularly useful marker for early detection of prostate cancer and in monitoring for disease progression.

Deflection-based cantilever sensors are good candidates for biological sensors since their ability of working in air or liquid can allow real-time analysis. However, their use in practical applications has been somewhat hindered by: the need of one-sided functionalization to induce differential surface stress and a lower sensitivity compared to resonant-based cantilever sensors (2.1.2). The latter one is because the typical deflection-based system requires very high surface coverage of analytes to induce measurable bending [13] while the resonant-based systems can detect single cell (2.1.2) [16].

2.1.2 Resonant-based Cantilever Sensors

2.1.2.1 Principles of Operation

Cantilevers possess a mechanical resonant frequency that is determined by their geometry and on the material being employed. When mass is adsorbed on such a cantilever surface, it causes a corresponding decrease in resonant frequency. The resonant frequency, f_o, of a resonant mechanical device can be characterized as a spring-mass system with the absence of damping [39]:

$$f_0 = \frac{1}{2\pi}\sqrt{\frac{k}{m}} \qquad (2.2)$$

where k is the spring constant and m is the effective mass of the resonator. When

a small mass, Δm, is added to the device, the resulting change in frequency, $\Delta f = f_{after} - f_0$, can be approximated to the first order by [39]:

$$\Delta f = -\frac{1}{2}\frac{\Delta m}{m} f_0 \qquad (2.3)$$

By rearranging Eq 2.3, the mass sensitivity, $\frac{\Delta m}{\Delta f}$ (g/Hz), of the resonator is

$$\frac{\Delta m}{\Delta f} = \frac{2m}{f_0} \qquad (2.4)$$

The general equation of the resonant frequency of the fundamental, out-of-plane mode of a cantilever (Eq 2.5) has been derived by Timoshenko [40] for numerous cross-sections;

$$f_0 = \frac{3.515}{2\pi}\frac{1}{L^2}\sqrt{\frac{EI}{\rho A}} \qquad (2.5)$$

where L is the cantilever length, I is the second moment of inertia (or area moment of inertia), ρ is the density of the resonator material, and A is the cross-sectional area of the beam. The second moment of inertia is a measure of the resistance of a cantilever to bending and deflection. For a typical rectangular cross section with width w and thickness t, the second moment of inertia is [41]:

$$I = \frac{wt^3}{12} \qquad (2.6)$$

As seen from Eq 2.2 - 2.6, a smaller resonant beam results in a lower mass sensitivity and, therefore, a smaller minimum detectable mass.

2.1.2.2 Applications

Resonance-based micro-/nano-cantilevers, or simply micro-/nano-resonators, demonstrated extremely high sensitivity for the detection of various chemical [3, 42-46] and biological [15-17, 47-52] analytes. As chemical sensors, detection of hydrogen gas was demonstrated on palladium-coated resonators [43] as well as PtO_2 film deposited resonators [44]. Also, Thundat *et al.* [45, 46] detected mercury vapour by using gold coated microresonators. Polyetherurethane-functionalized resonators were used to detect octane and toluene vapours at concentrations in the single ppm range [3, 42].

Resonant devices have also shown promising sensitivity to measure extremely small masses in vacuum where the quality factor degradation due to viscous damping is avoided (Sec. 2.1.2.4). Ilic *et al*. [48] have detected 6.3 attogram (ag) of thiol self assembled monolayers on the gold dots patterned onto a paddle-nanoresonator and estimated the smallest resolvable mass with their devices to be 0.39 ag. Detection of thiolated single dsDNA molecule (1587 bp) with a mass of 1.65 ag was also demonstrated using nanoresonators functionalized with localized gold nanodots [49]. This was done by observing many cantilevers which revealed approximately discrete frequency jumps corresponding to a handful of DNA molecules. Normalizing these shifts to the frequency shift from a single binding event enables counting of DNA molecules bound to a particular cantilever.

Although the deflection-based cantilevers are more commonly used as biosensors due to their ability to operate in fluid environments, some recent works have demonstrated the improved operation of resonators in air or liquid. Lee *et al.* [51] and Hwang *et al.* [17] have detected PSA at concentrations of 10 pg/mL at atmospheric pressure and 1 ng/mL in liquid using calixcrown self-assembled monolayers on gold-coated nanoresonators. Detection of individual *E. Coli* in air has been demonstrated by Ilic *et al*. [16, 52].

2.1.2.3 Quality Factor

The mechanical quality factor (Q factor) is a measure of the energy dissipation and the performance of a resonant MEMS/NEMS device. Mathematically, the Q factor is defined as the ratio of the resonance frequency, f_o, to the full width of the resonance peak evaluated at the half-maximum (FWHM = full width half-maximum) as shown in Figure 2.2. The definition of the Q factor is given by [54]:

$$Q = \frac{f_0}{FWHM} \qquad (2.7)$$

Sharper peaks (e.g. the decreasing width at FWHM) render higher resolution of peak frequency shifts. The Q factor is directly related to the sensitivity of the resonant device since an increase in Q lowers the minimum detectable frequency and thus the minimum detectable mass.

The Q factor of a resonant device is affected by numerous losses and each of those losses individually contributes Q factor according to the following equation [60]:

$$\frac{1}{Q_{total}} = \sum \frac{1}{Q_{individual}} \qquad (2.8)$$

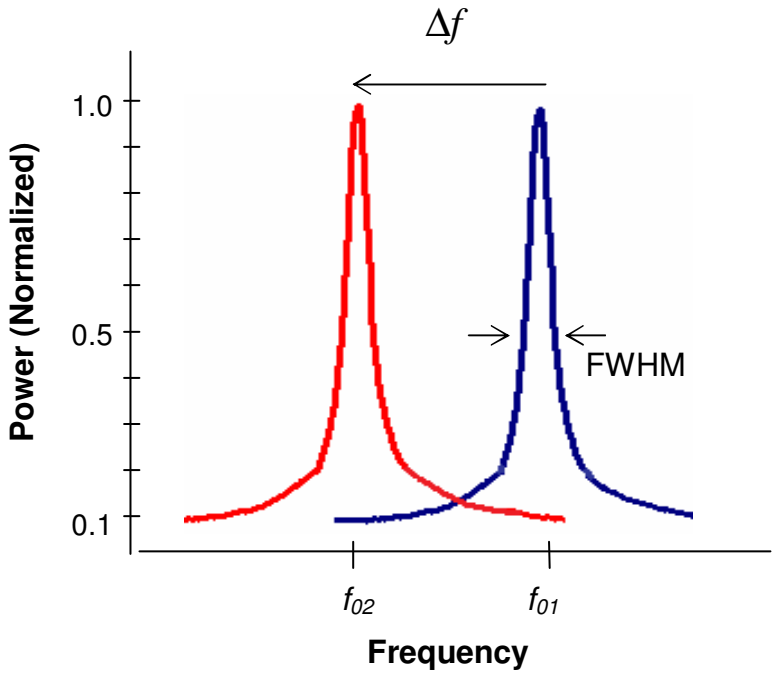

Figure 2.2: Generic frequency response curves

Therefore, the overall Q factor, Q_{total}, is limited by the lowest Q factor of all. The following section will focus on the three main loss mechanisms, namely thermoelastic loss, support loss and loss due to air damping.

2.1.2.4 Factors Influencing Q Factor

Thermoelastic Energy Dissipation (TED)

When the resonator structure is deformed, the strain gradient induces a temperature gradient. This induced gradient yields energy dissipation due to irreversible heat flow and consequently relaxation of the structure back to its equilibrium [56-58]. This fundeamental process known as thermoelastic damping would ultimately limit the quality actor achievable by micro- and nanoscale resonators. Theoretical and experimental studies have shown that the TED-related limit on quality factor depends on the resonator dimension, material, and working temperature [59-62]. However, as device dimensions reach the

submicron scale, extrinsic dissipative processes such as surface-related phenomena and clamping point effects will dominate the performance of the device, limiting their quality factor to values several orders of magnitude lower than the TED-limited value. [59, 60].

The approximation of the TED-limited Q can be made using a thin rod transversal vibration model [60]. In case of commonly used rectangular cantilevers, the rod diameter in the model is replaced by the cantilever thickness as follows:

$$Q_{TED} = 80\frac{\chi}{ft^2}\frac{E}{\delta E} \qquad (2.9)$$

$$\delta E = E_{ad} - E = \frac{E^2 T\alpha^2}{9c_P} \qquad (2.10)$$

$$\chi = \frac{\kappa}{\rho C_P} \qquad (2.11)$$

where:

f = the resonance frequency [Hz]
t = the thickness of the beam [m]
χ = the thermal diffusivity [m^2/s]
κ = the thermal conductivity [W/(m-K)]
C_P = specific heat capacity [J/(kg-K)]
ρ = density [kg/m^3]
E = the isothermal Young's modulus [N/m^2]
δE = the difference between the adiabatic
E_{ad} and the isothermal Young's moduli [N/m^2]
T = absolute temperature [K]
α = thermal expansion coefficient [1/K]

Support Loss

In vacuum, the Q factor becomes generally limited by support losses [60]. Mechanical structures are not perfectly rigid in reality, and, energy can be dissipated to the support structure where local deformations and microslip can occur when the resonator structure vibrates [41]. Yang *et al*. [60] reported that support loss in an ultrathin cantilever will dominate for structures with a length (L) to thickness (t) ratio of less than 100 (i.e. L/t < 100). Park *et al.* [65] developed a computational model to predict wave propagation in the substrate of a MEMS resonator to study energy loss mechanisms from the vibrating beams to the support. By varying the beam length, support loss was predicted to increase a hundredfold for every tenfold increase in resonator center frequency in doubly-clamped resonators.

The energy dissipation to the support can be calculated according to a two-dimensional theory of elasticity by modeling the support as an infinitely large elastic body in comparison to the size of a cantilever [66]. For the first-mode resonance, the support loss limited Q factor can be estimated from the following equation [60, 66]

$$Q = 0.34\left(\frac{L}{t}\right)^3 \qquad (2.12)$$

Surface Loss

Surface loss is another dominant loss mechanism in vacuum for micro-/nano-scale resonators. As the resonator thickness scales down, the surface-to-volume ratio increases and the effect of surfaces becomes dominant. Resonator surfaces may have impurities, lattice defects, absorbents or other imperfections which serve to dissipate energy. A quantitative model for this loss has not yet been fully developed but experimental demonstrations have shown that surface treatments, such as annealing, can minimize these surface imperfections so that quality factor dramatically increases [60,66].

Air Damping

MEMS/NEMS resonating in the out-of-plane mode at ambient pressures are subject to resistance from the surrounding fluid. This fluid-induced effect, also known as viscous damping, is often a dominant loss mechanism in non-vacuum environments and increases with pressure in air or with increasing beam's surface-to-volume ratio [13, 63, 67-70]. It is not uncommon to experience a reduction in Q factor of two to three orders of magnitude when operating in air rather than vacuum [13, 69]. The analysis of pressure-dependent damping of a resonating beam can be done by dividing the pressure ranges into four regions [63, 67, 69, 70].

In the first region, the intrinsic damping region, the pressure is so low that air damping is negligible compared to other loss mechanisms. The intrinsic Q factor is independent of pressure and must be determined empirically since the quantitative model for surface loss which is a dominant source of energy loss in vacuum has not yet been developed and, therefore, cannot be mathematically estimated [71].

In the second region, the molecular region, air damping is the dominant mechanism but air molecules are so far apart that they do not interact with each other [60]. In this region, the air damping is proportional to air pressure and the Q factor for a standard cantilever beam is given by [69]:

$$Q = \frac{2\pi f_n t \rho}{k_m P} = \frac{k_n^{\,2}}{k_m P}\left(\frac{t}{L}\right)^2 \sqrt{\frac{E\rho}{12}} \qquad (2.13)$$

$$k_m = \sqrt{\frac{32M}{9\pi RT}} \qquad (2.14)$$

where:

f_n = resonance frequency of the n^{th} mode [Hz]
ρ = density of the cantilever [kg/m^3]
P = pressure [Pa]
k_n = constant of the n^{th} mode resonance
t = thickness of the cantilever [m]
L = length of the cantilever [m]
R = universal gas constant [J/mol.K]
T= Absolute temperature [K]
M = molar mass of the air [kg/mol]
k_m = [s/m]

The third region is the crossover region where neither viscous nor free molecular flow adequately describes gas behaviour [63, 70]. This region is defined as 0.01<< Kn << 10 where the Knudsen number, Kn, measures the ratio of the mean free path (λ_{mfp}) of gas molecules to the size of the beam (w) ($K_n = \lambda_{mfp} / w$).

The fourth region is the viscous region. The pressure is high enough that the air molecules do interact with each other, and the air is assumed to act as a viscous fluid. In this region, Q factor is inversely proportional to the fluid viscosity (μ) [71]. The Q factor in this region is estimated using Stoke's law for damping [72]:

$$Q = \left[\frac{w(E\rho)^{1/2}}{24\mu}\right]\left(\frac{t}{L}\right)^2 \qquad (2.15)$$

where:

E = Young's modulus [N/m^2]
ρ = fluid density [kg/m^3]
t = thickness of the cantilever [m]
L = length of the cantilever [m]
w = width of the cantilever [m]

Therefore, the value of the Q factor is strongly influenced by the media that surrounds the cantilever in the viscous regime.

2.1.2.5 Actuation Mechanisms

A resonant cantilever is often excited at its resonance frequency to obtain a measurable signal. Several approaches have been used to perform this actuation: magnetic, electrostatic, piezoelectric and photothermal.

Magnetic Actuation

A cantilever can be actuated by placing it in a magnetic field. As shown in Figure 2.3. (A), a cantilever plane with a magnetic layer can be placed perpendicular to an external magnetic field, B, induced by a coil [3, 73]. Application of an alternating current through the coil induces the magnetic field which then exerts a transverse force on the cantilever. The force, F, acting on the cantilever with length L can be calculated using the formula $F = m_C B/L$ [73] where m_C is the magnetic dipole moment of the cantilever.

A cantilever with a conductive pathway can be electromagnetically actuated by placing it in a constant external magnetic field [42, 74] (Fig 2.3 (B)). Application of an alternating current I to the conductor on the cantilever generates a transverse Lorentz force $F_L = 2IbB$ where b denotes the active section of the current path perpendicular to the magnetic field [42].

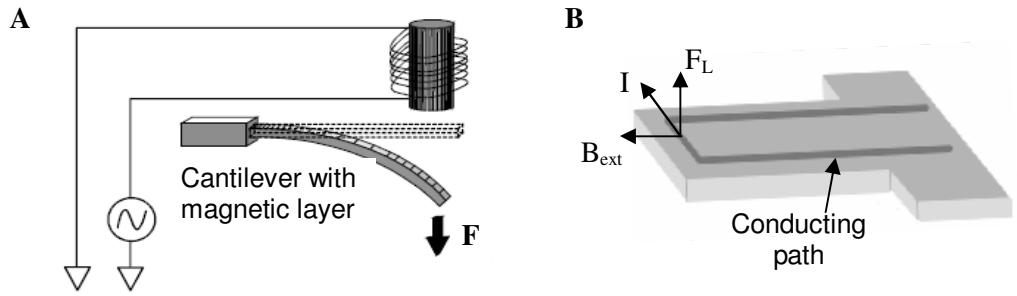

Figure 2.3: Example of (A) magnetic actuation (Reprinted with permission from ref [3]. Copyright Elsevier, 2006) (B) electromagnetic actuation

Magnetic or electromagnetic excitation can be achieved with relatively low power consumption and the excitation frequencies can be extended to several megahertz. However, the integration of a magnetic field and an electric pathway complicates the fabrication and the packaging of the devices.

Electrostatic Actuation

A cantilever can also be driven by electrostatic forces. The electrostatic force, also known as the Coulomb force, consists of the attractive or repulsive force between two charged particles. Applying an alternating voltage between the cantilever surface and the underlying substrate generate electrostatic forces and results in the actuation for the structure [75, 76].

Piezoelectric Actuation

A piezoelectric material is a material that produces mechanical deformation, i.e. shrinkage or expansion, when an electrical field is applied. Cantilever actuation can be performed by depositing a thin layer of piezoelectric material such as lead zirconate titanate (PZT) and polysilicon onto the device and applying a sinusoidal voltage [51, 77]. Alternatively, a cantilever chip can be simply attached to a piezoelectric actuator to induce resonance [16].

A piezoelectric cantilever has the advantage of simultaneous electrical excitation and detection of the mechanical resonance using a feed back circuit. Also, it can be easily integrated with a lab-on-a-chip because external hardware or equipment is not needed. However, it generally requires additional conductive layers on the oscillator surface, which, in turn, reduces the quality of the resonance [78]. Also, fabricating the electrical connection to the individual cantilever in arrays can be complicated.

Photothermal Actuation

When heat is passed through a stack of materials with different thermal expansion coefficients, stresses are built between the layers and result in bending motion. Photothermal actuation is a method of thermally driving resonance using a laser beam as a localized heat source. A laser beam modulated at device resonance is focused on the cantilever's clamped end, typically consisting of a thin silicon or silicon nitride device layer and a sacrificial silicon oxide layer underneath. The difference in the thermal expansion coefficients of these layers generates a periodic compressive and tensile stresses which again drives the free end of the cantilever beam in resonance [78, 79].

Photothermal actuation offers easy implementation since electrical connection to the device is not required. It is also easy to integrate with an optical interferometric resonance detection system. The disadvantage of photothermal actuation is that an external laser is needed, which has not been integrated on a chip and therefore it may increase the costs and dimensions of the system [19].

2.1.3 Fabrication Techniques

Fabrication of micro-/nano-cantilevers is based on two distinct micromachining strategies: (a) bulk micromachining and (b) surface micromachining [13, 80]. Bulk micromachining is used to create suspended structures by removal of substantial portions of the substrate. Surface micromachining uses the original substrate as a base for another layer in which the device is fabricated. Both strategies involve common fabrication processes such as thin film deposition, photolithography, doping substrate and etching. These are well established technologies commonly used in fabricating integrated circuits. For in-depth information of these techniques, please refer to ref. 85 and 86. The most commonly employed substrate is single crystal silicon with silicon oxide, silicon

nitride, polycrystalline silicon (polysilicon) and metal films used as device layers. Polymers have also been used to fabricate static cantilevers since polymers can provide much larger beam deflection to give, in turn, better sensitivity for given amount of surface stress [81-83].

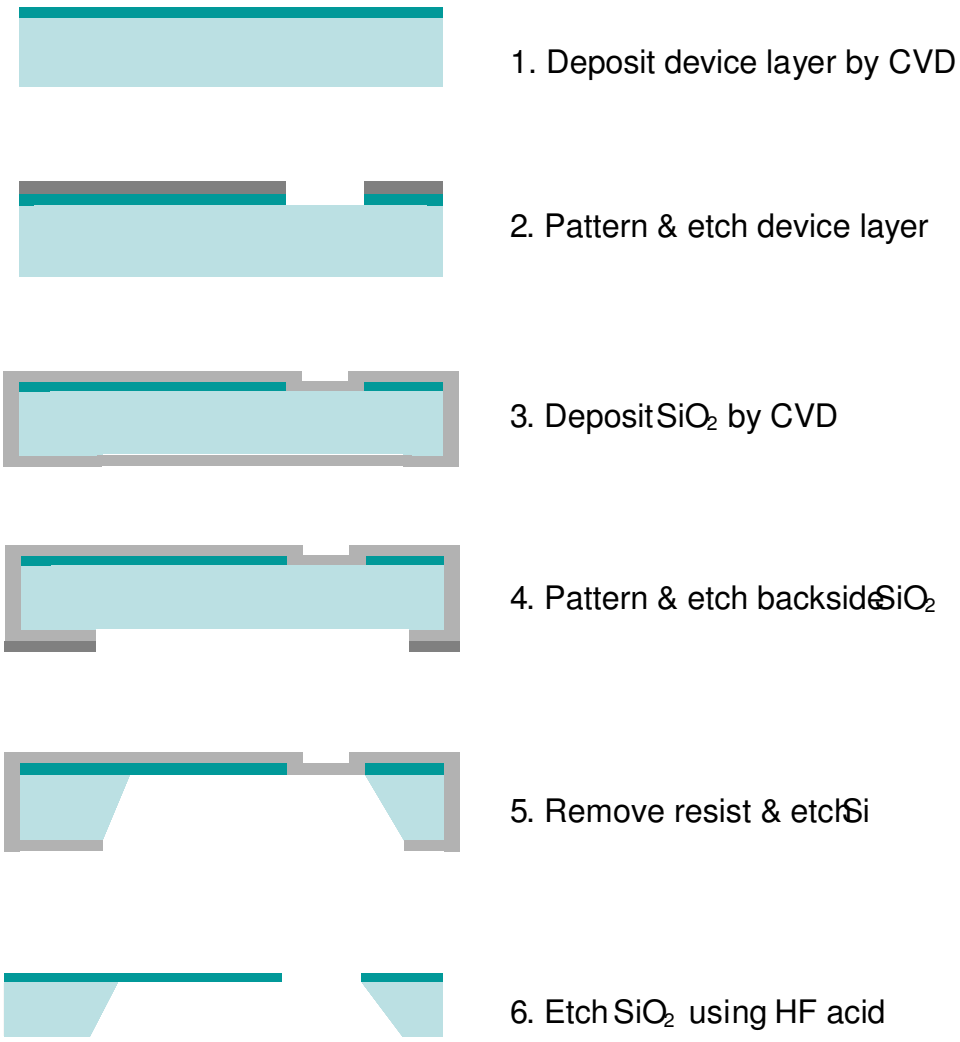

Figure 2.4: Bulk micromachining process flow

2.1.3.1 Bulk Micromachining

Bulk micromachining is a subtractive technique in which a Si substrate is used as the sacrificial layer [13, 84]. Figure 2.4 shows the overall bulk micromachining process for a silicon cantilever. First, a thin device layer is deposited on the Si substrate using chemical vapour deposition (CVD) (Fig 2.4 (1)). The cantilever shape is patterned on the photoresist-coated wafer and a trench around the cantilever is etched by a reactive ion etching (RIE) technique (Fig 2.4 (2)). Following the resist removal, a thin layer of silicon dioxide is deposited around the wafer by CVD (Fig 2.4 (3)) and the layer on the backside of the wafer is patterned and etched to make a trench (Fig 2.4 (4)). After removing the resist, the exposed backside of the silicon substrate is anisotropically etched in potassium hydroxide (KOH) or tetramethyl ammonium hydroxide (TMAH) [13] to release the cantilever (Fig 2.4 (5)). KOH and TMAH can selectively etch Si over SiO_2 with a high ratio. The device layer is typically an implanted dopant layer or a thin film deposited on the substrate, that are resistant to the anisotropic etching.

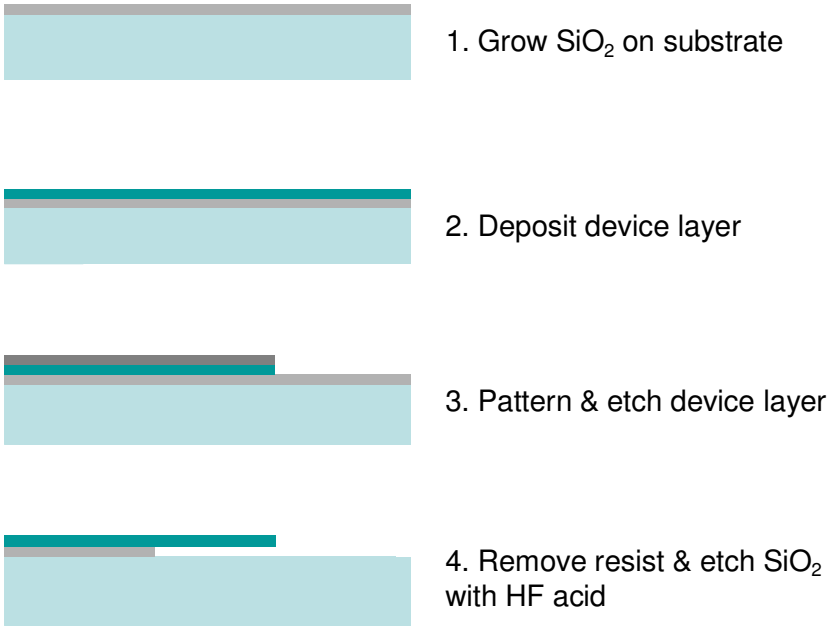

Figure 2.5: Surface micromachining process flow

The oxide layer around the wafer is finally etched in hydrofluoric (HF) acid (Fig 2.4 (6)).

2.1.3.2 Surface Micromachining

Surface micromachining is an additive technique in which a sacrificial layer is grown on a silicon substrate followed by a deposition of a device layer. Figure 2.5 depicts the overall surface-micromachining process for a silicon cantilever. A SiO_2 sacrificial layer is grown on the silicon substrate (1) followed by a deposition of a device layer through CVD (2). The device layer is then patterned with resist and etched using a reactive ion etch (3). Finally the device layer is released by undercutting the sacrificial layer with HF acid (4).
Surface-micromachining involves a fewer processing steps than bulk-micromachining. However, the close proximity of the device to the silicon substrate can result in *stiction* whereby the cantilever structure is not released but stuck to the substrate [13]. This occurs due to the surface tension forces of the liquid when drying the liquid in the space between the substrate and the structural layer. Critical point drying can instead be used after step of releasing the device layer to prevent stiction [13].

Cantilevers can also be surface-micromachined using silicon-on-insulator (SOI) wafers. SOI wafer are composed of a thick bottom substrate layer of single-crystal silicon, a middle buried silicon oxide layer and a top device layer of single-crystal silicon or silicon nitride [86]. SOI wafers are readily available with a device thickness of tens to a few hundred nanometers and with a buried oxide layer thickness of up to a few micrometers. Fabrication on SOI wafer is useful as fewer processing steps are necessary and an etch stop is already available.

2.2. Microfluidic Immunoassays

Immunoassays are some of the most important analytical techniques and have been widely used in clinical diagnoses, environmental analyses and biochemical studies. They present one of the simplest methods of identifying and measuring protein presence and concentrations [8]. The basis of immunoassays is the sensitivity and specificity of the antibody-antigen interaction and this has shown the capability of detecting a broad variety of clinically important analytes like disease biomarkers, hormones, antibodies, viruses, bacteria and pollutants present in biological samples [87]. A conventional immunoassay is carried out in 96-well microtiter plates and involves a series of mixing, reaction and washing steps, which not only are laborious but also often lead to large errors and inconsistent results [88, 89]. Also, several hours are required to complete one assay due to the long incubation time required in each step. However, these problems can be solved by a microfluidic immunoassay. Microfluidics are optimal for this application due to automation, lesser required volume of reagents which leads to reduction of cost, shortened analysis time, and potential portability. In the following sections, reviews on material and techniques of surface modification, fluid handling and detection used in microfluidic immunoassays are presented.

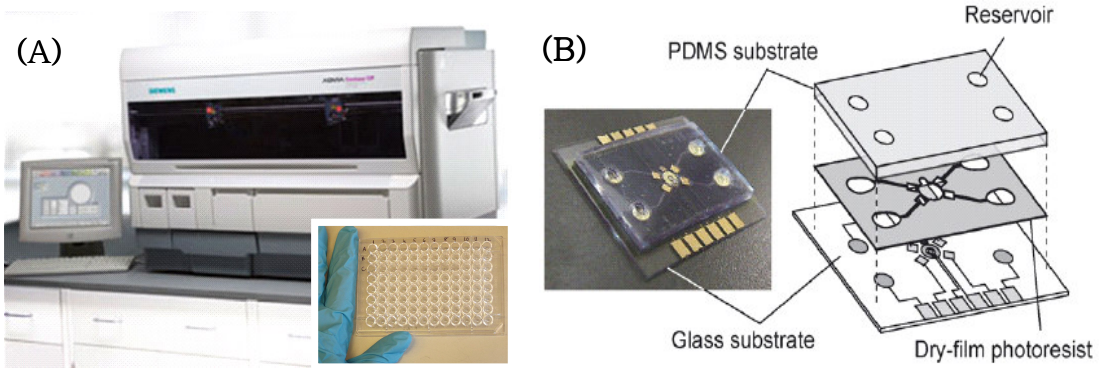

Figure 2.6: Immunoassay systems (A) conventional microtiter-plate based immunoassay system (Siemens) (B) integrated microfluidic chip (22 mm x 17 mm) for immunoassay. Reprinted with permission from ref [2]. Copyright Elsevier, 2007.

2.2.1 Material

The surface chemistry and optical transparency are two major considerations for materials used in microfluidic devices. The surface property of the material is a dominant factor for the surface modification and fluid handling within the chip, and the optical property of the material governs the detection mode of immunoassays [9].

Silicon was frequently used as a substrate in the early stage of microfluidic development. Silicon-based devices take advantages of an extremely well established technology for a nanometer scale fabrication and well characterized physical and chemical properties. In addition, the surface chemistry of silicon and silicon dioxide layer has been extensively studied and many techniques exist to attach molecules and coatings on silicon substrates [10]. However, its non-optical transparency in the UV/visible region is not suitable for the commonly used optical detection methods in microfluidic devices (2.2.4) and the requirement of an expensive fabrication facility consequently limits its use towards commercialization [9].

Glass has been a standard material for most immunoassay applications in replacement of silicon. Although more fragile than silicon, glass substrates offer excellent optical properties throughout the visible spectrum. Glass has been employed in applications such as microchip capillary electrophoresis and immunoassay involving electrochemical detection [9]. However, glass fabrication requires extensive microfabrication facilities, much as silicon.

In contrast, polymer substrates are attractive materials due to ease of microfabrication under normal laboratory conditions as well as optical transparency and good chemical resistance. Polydimethylsiloxane (PDMS), Polycarbonate and polymethymethacrylate (PMMA) are commonly used polymer substrates in microfluidic immunoassays. In particular, PDMS is used

extensively and can produce feature sizes as small as 10 nm [90]. The elastomeric nature of the material makes it amenable to low pressure applications as it seals well to form microchannels. In addition, PDMS can be bonded irreversibly to itself, glass or silicon by treating both bonding surfaces with an oxygen plasma [10, 91].

2.2.2 Surface Modification

Device miniaturization offers advantages of low cost due to reduced amount of reagent volume and shortened analysis time. However, the increased surface-to-volume ratio with miniaturization can cause a major problem of degrading the immunoassay efficiency due to the non-specific binding of the key reagents to the surface of material [88]. Biomolecules such as antibodies have been known to non-specifically adsorb to a hydrophobic surface. This adsorption often causes protein denaturation and reduces their activities by more than 90% [92-94]. Control over surface properties is therefore required. Bovine serum albumin (BSA) has been commonly used to prevent the non-specific adhesion of proteins on microchannel surfaces. However, its non-permanency and the resulted heterogeneity motivated alternative approaches such as the modifications through surface chemistry [9, 10]. Chemical surface modification using covalent bonding between specific biocompatible reagents and material surface has provided uniformly oriented antibody immobilization leading to homogenous antigen-antibody binding [95].

There have been considerable efforts in surface modification of polymer materials compared to silicon and glass. Polymer surfaces are generally hydrophobic, and proteins and other molecules tend to adsorb to their untreated surfaces. For improvement of the assay performance, Bai *et al.* [88, 96] treated the PMMA surface of the microchannel on the microfluidic device with an amine bearing hydrophilic polymer, polymer(ethyleneimine) (PEI) and achieved a

tenfold increase of active antibodies than those with an untreated PMMA surface. The PDMS surface can be temporarily made hydrophilic through oxidation by either UV exposure [97, 98], oxygen plasma treatment [98] or CO_2-pulsed lasers for polymerization and grafting of vinyl monomers [99]. Currently explored methods to produce stable hydrophilic surfaces includes polymer grafting [100, 101] and chemical functionalization with covalent bonding of poly(vinyl alcohol) on a silanized PDMS [102], and implementation of a small amphipathic fungal protein called hydrophobins [106]. Recently, the use of supported bilayer membranes (SBMs) has attracted considerable attention for surface modification and functionalization. The SBM is a biointerface in which a single lipid bilayer is attached to the solid substrate by physical interactions or chemical bonds. Phillip *et al.* [103, 104] utilized phosphatidylcholine membranes assembled on plasma-oxidized PDMS by vesicle fusion and achieved a reduction of 2-3 orders of magnitude in nonspecific adsorption of avidin and BSA, as compared to that on only plasma oxidized surfaces.

2.2.3 Fluid Handling / Delivery

The common methods for delivering fluids in microchannels are the pressure- [107-118] and electrokinetic- [90, 119-124] driven flows. In pressure-driven flow, reagents are typically delivered to the inside of the microchannel by using the pressure gradients along the channel. These gradients can be created either by applying a vacuum at the outlet while opening the inlet to atmospheric pressure or by applying a pressure at the inlet while opening the outlet to atmospheric pressure. This can be done by using a syringe pump or vacuum [118]. Pressure-driven flow takes advantage of being effective for a wide range of solutions including non-electrically conductive fluids. However, its traditional mechanism requires an external pump or a vacuum source (i.e. syringe pump or vacuum) which can make the device bulky and less portable. Microvalves that can be integrated into a chip have thus been developed by exploiting the elastomeric

property of PDMS. Quake and co-workers [107, 108] and Grover *et al.* [109] used PDMS as a deflecting thin membrane to fabricate a pneumatically actuated valve and formed a peristaltic pump by arranging three valves in a row.

Passive fluid handling techniques such as capillary pump [111-117], gravity-induced flow [125] and air-evacuated PDMS pumping [110] have been gaining attention due to their simplicity and ease of operation. In the case of capillary pumps, spontaneous filling of the channel is induced by the interplay between the surface tension of the liquid and the chemistry and geometry of the channel walls [7-10]. Delamarche *et al.* [115] used capillary action in plasma-oxidized PDMS to deposit immunoglobulins onto a surface. Juncker *et al.* [117] developed a microfluidic capillary system that autonomously transports aliquots of different liquids in sequence to perform a sandwich immunoassay for C-reactive proteins. These passive fluid delivery techniques do not require any external power supply or control device and are geared towards reinforcing the realization of a complete automation for a point-of-care type chip.

Electrokinetically driven flow is a well-established method amenable to automation [10]. This flow is based on electroosmosis which results from the movement of charged molecules in an electric field. In glass microchannels or plasma-oxidized PDMS-based microchannels, a thin layer of cation-enriched fluid forms at the surface of negatively charged silanol groups of the channel wall [90]. The layer of cations is driven towards the negatively charged cathode when an electric potential is applied to the channel and the motion is transferred to the rest of the liquid through viscous drag. Electrokinetic-driven flow takes advantage of the easy fluid flow control through an automatic switching module, but is limited to the use of conductive liquids. The need for an off-chip power supply and evaporation of solvent due to heating are other disadvantages. Dodge *et al.* [124] were the first to report an electrokinetically-driven immunoassay within a microchannel network where immunoglobulin (IgG) was tested on surface-immobilized Protein A. Linder *et al.* [122, 123] employed electrokinetic

sample transport to perform a sandwich immunoassay for human IgG. Gao *et al.* [120, 121] and Hu *et al.* [119] have developed electrokinetically-controlled immunoassay chips made of PDMS-coated glass for the detection of multiple analytes such as *Helicobacter pylori* and *E. coli* and achieved detection limits as low as 3 μg/mL of *E. coli*.

2.2.4 Detection

Detection techniques can be classified as labelled and label-free detections. Most applications use a label to increase the sensitivity of detection. Fluorescence and electrochemical methods are currently the two dominant label-based detection techniques. Surface plasmon resonance (SPR) is a common label-free detection approach that has also been implemented in microfluidic devices.

The most common detection method used in immunoassays is fluorescence, primarily due to its high sensitivity and the ease of use. Fluorophores and enzyme-labeled antibodies/antigens are two common conventional label-based techniques. Immunocomplex formation can be monitored by direct fluorescence observation when an antigen interacts with a fluorophore-labeled specific antibody [9]. Enzymes are powerful labels because they act as biological catalysts and result in the acceleration of various biological reactions [126]. The advantages of working with enzymes include high catalytic activity, selectivity and the sensitivity especially when used in sandwich immunoassays such as enzyme-linked immunosorbent assays (ELISAs) in which antigen in the unknown is bound to the pre-immobilized antibody site, then enzyme-labeled antibody is bound to the antigen. Eteshola *et al.* [127] developed a PDMS microfluidic device to perform ELISAs for sheep IgM and achieved a sensitivity reaching 17nM. Integration of other signal amplification strategies can further enhance signal sensitivity [128-130]. Shin *et al.* [128] demonstrated a C-reactive protein (one of the acute phase proteins found in the blood in response to

inflammation) immunoassay with 20-fold amplified fluorescence intensity using microbeads as solid substrates for the primary antibodies. Microbeads can enhance the sensitivity of assays by improving surface to volume ratio for reactions and thus boost the efficiency of sample-reagent interactions.

Electrochemical detection is the second most commonly used method and often uses an enzyme or an electroactive molecule as a label. Electrochemical detection is typically performed through amperometry by measuring the current as a function of time while the potential at the electrode is held constant. Rossier *et al.* [131] presented a polymeric microfluidic device with an integrated electrode for ELISA to detect D-Dimer, an important element of the blood coagulation mechanism, with a detection limit of 100 pM. Some significant merits of electrochemical detection are easy miniaturization and low power requirements. However, the miniaturization-accompanied decrease in current requires the improvement of electronics and/or shielding to allow for low current measurement and stability of a reference electrode [10]. Improved sensitivity can be achieved by using an amplified electromechanical transducing system, such as an interdigitated array (IDA) electrode to allow for the regeneration of electroactive species [87]. This system include two working electrodes, each of which is an array of planar and parallel metal fingers, which are interdigitated but separated by insulating material. When the potential of each set of electrodes is controlled individually, a species oxidized at one electrode can be reduced at the neighbouring electrode, making the molecule available for a subsequent re-oxidation.

Label-based microfluidic immunoassays possess drawbacks [132]. First, chemical labelling of proteins may change their surface characteristics so that their physical activity is impaired. Labels are connected to antigens or antibodies in a random way, and, depending on the binding site, the labels could interfere with the function of the protein, reducing its chemical activity. Secondly, the varying labelling efficiency for different proteins makes accurate quantification

of the results difficult. Thirdly, the labelling procedure is time consuming and labour intensive. In addition, labelled detection especially fluorescence technique becomes increasingly difficult due to sensitivity being not enough to distinguish very few fluoresced photons from the background as the detection limits enters ng/mL ~ pg/mL concentration [13]. In effort to overcome the aforementioned problems, there have been a rising number of reports on label-free detection implemented within microfluidic immunoassays. Surface plasmon resonance (SPR) has been widely used as a label-free technique for a variety of chemical and biochemical applications (Fig. 2.7). Lee *et al.* [134] have developed a SPR-based IgG immunosensing chip which includes arrayed microchannels, micro-pumps and -valves, flow and temperature sensors and heaters. The detection limit obtained was 10 ng/mL. In addition, Kurita *et al.* [135] demonstrated an on-chip enzyme immunoassay for B-type natriuretic peptide (BNP), a cardiac marker, using microfluidic device combined with a portable plasmon resonance system, and achieved 5 pg/mL of BNP. Other interesting microfluidic label-free detections include quartz crystal microbalance (QCM) and MEMS cantilever sensors. Immunological receptors are immobilized on the quartz wafer electrode or the resonator surface and the presence of target proteins is determined by monitoring the shift in the resonance frequency due to surface-adsorbed mass of the target proteins. Michalzik *et al.* [136] presented a miniaturized QCM microfluidic system which detected 0.5 μg/mL anti-protein A by coating the quartz substrate with 2 μg/mL protein A. Detection of prostate-specific antigen (PSA), a biomarker for prostate cancer, using microcantilevers integrated in microfluidic cells has been demonstrated in static [37, 38] and dynamic [16] mode of operation with the overall sensitivity of 0.2 ng/mL obtained in liquid.

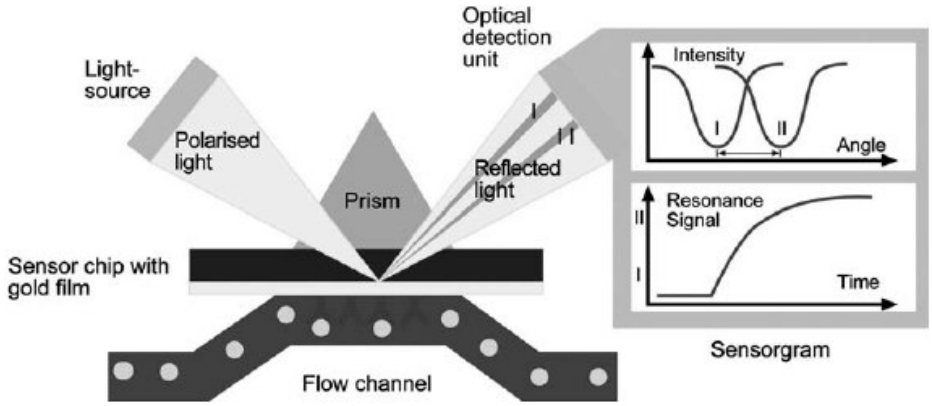

Figure 2.7: Typical set-up for a surface plasmon resonance biosensor. Typically a thin gold-film is coupled to a glass prism and a plane polarized light is directed through a glass prism to the gold/solution dielectric interface over a wide range of incident angles. The intensity of the resulting reflected light is measured against the incident light angle with a detector. At certain incident light wavelength and angles, a minimum in the reflectivity is observed at which the light waves are coupled to the oscillation of surface plasmons at the gold/solution interface. The angle of the minimum in reflectivity is denoted as an SPR angle. The SPR angle shifts (from I to II in the diagram) when biomolecules bind to the gold surface and change the mass of the surface layer. This change in resonant angle can be monitored non-invasively in real time as a plot of resonance signal (proportional to mass change) versus time. Reprinted with permission from ref [156]. Copyright Springer, 2003.

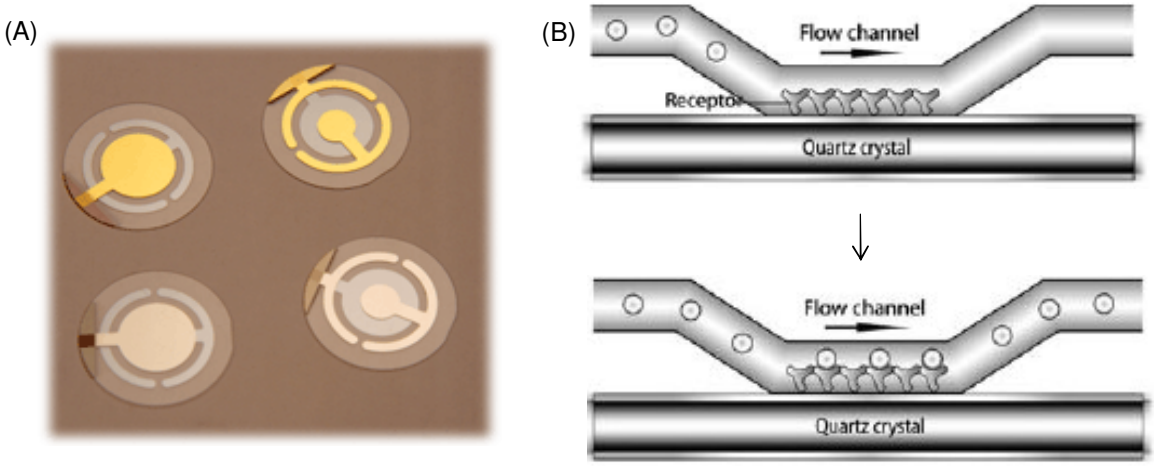

Figure 2.8: (A) Quartz crystal microbalances. (B) A quartz crystal resonator coated with a receptor integrated into a flow cell to which target molecule can be added. As liquid is passed over the surface the crystal resonates giving a signal. Reprinted with permission from ref [156]. Copyright Springer, 2003.

Chapter 3

Microchip Design and Fabrication

This chapter describes the design and fabrication of an integrated MEMS-fluidic device developed in this thesis. The 2.5 cm by 1.2 cm device chip consists of a 1 cm by 1 cm silicon nanoresonator chip and a tri-layer of glass-PDMS-glass structure for integration of micro pneumatic valves and pumps. The nanoresonators with the thickness of 340 nm and the width of 700 nm are designed to operate at 4.5 MHz ~ 10 MHz, depending on the resonator length (6.8 μm ~ 10.5 μm). The ability of the resonators in the system to resist stiction is also investigated by treating the device with liquid.

3.1 Design and Fabrication

3.1.1 NEMS Resonators

Figure 3.1 summarizes the surface micromachining technology used to fabricate the resonating devices. The fabrication process was performed at the University

of Alberta Nanofabrication facility. Arrays of nanoresonators were fabricated on (100) silicon-on-insulator (SOI, Soitec) substrate with a 340 nm thick device layer and a 1 µm thick buried oxide layer. First, a 4 inch SOI wafer was diced into 1cm x 1cm small chips and cleaned in hot Piranha (3:1 H_2SO_4:H_2O_2) for 20 minutes to remove any residual organics. Electron beam resist, PMMA 950K A2 (Microchem), was spun onto the chip at 500 rpm for 10 s and 4000 rpm for 40 s. The chip was then baked on a hot plate at 200 ^oC for 5 min to remove any residual solvent. Electron beam lithography (EBL, Raith 150) was used to pattern the resonators on the chip with an accelerating voltage of 10 kV, an aperture of 20 µm and an electron dose of 125 C/cm^2. The pattern was developed with a solution of 3:1 IPA : MIBK (Microchem) for 30 s followed by a 15 s IPA rinse. Areas of the device layer exposed in development were then anisotropically dry-etched in an ICP-RIE at a chamber pressure of 20 mTorr using gas flows of 80 sccm C_4F_8 and 110 sccm of SF_6. After the dry-etch, the

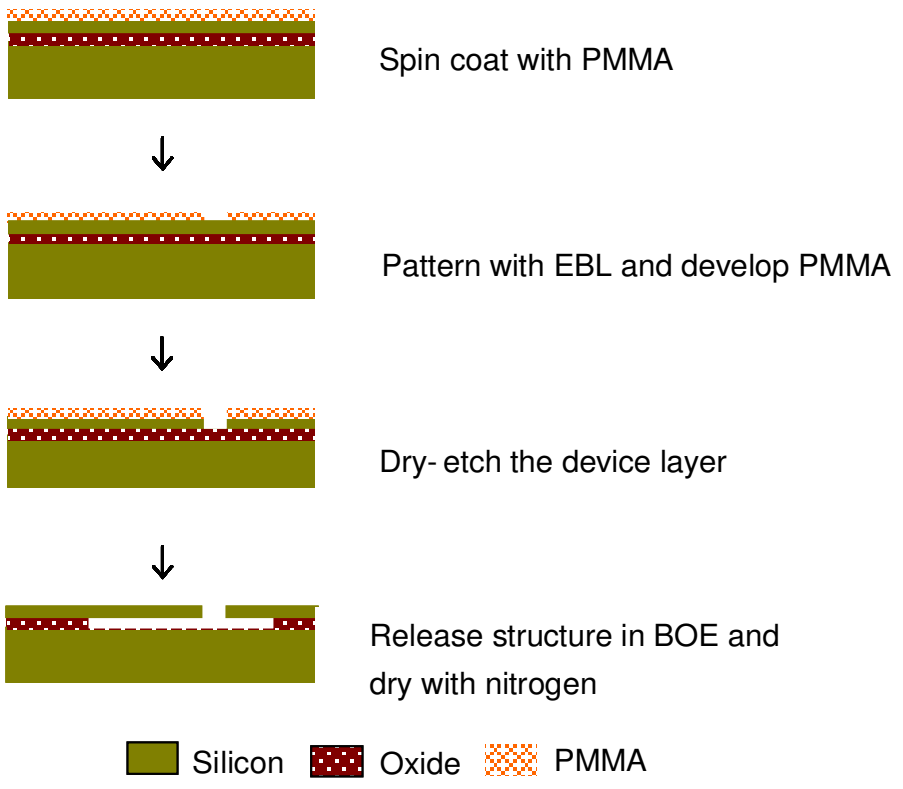

Figure 3.1: Fabrication process flow of silicon Nanoresonatorson SOI wafer

remaining PMMA was stripped with acetone and the nanoresonators were released by removing the sacrificial oxide layer in a buffered oxide etchant (BOE, 10:1 ammonium fluoride:hydrofluoric acid) for 24 min followed by a deionized (DI) water rinse. Lastly, the sample was dried using only a nitrogen gun. A critical point drying step was not required since the device did not experience stiction mainly because of the thick buried oxide layer that provided far apart distance between the device layer and the base layer. The resulted nanoresonators were 340 nm thick, 700 nm wide and 6.8 μm, 9 μm, and 10.5 μm long on average including approximately 700 nm undercut, and each chip includes 6 x 3 arrays of resonators at each beam length (Fig 3.2).

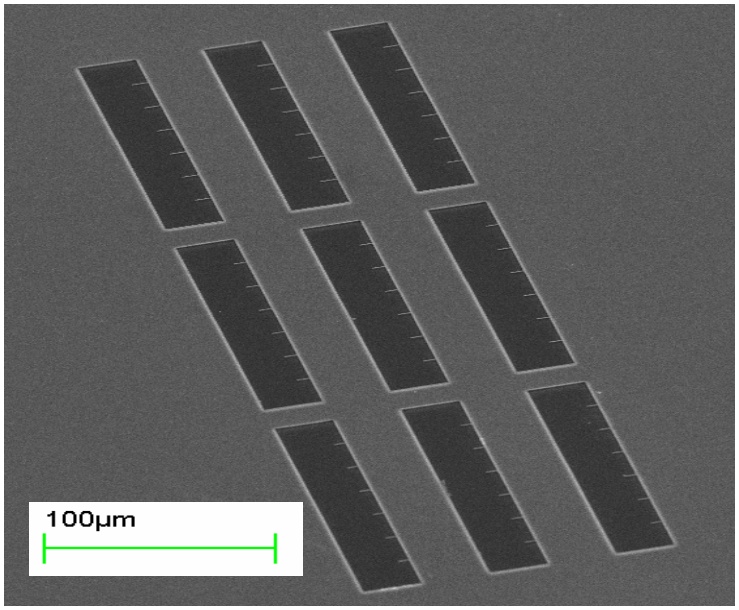

Figure 3.2. SEM of arrays of nanoresonators

3.1.2 Tri-layer Fluidic Structure

A micro pneumatic valve and pump based on tri-layer architecture were integrated in the chip for automated sample delivery. These were originally developed by Grover *et al.* [109] and subsequently modified by Kaigala *et al.* in the Applied Miniaturisation Laboratory [137]. The valve structure consists of a

top glass layer (control layer), a bottom glass layer (flow layer) and a PDMS layer between these two layers (Fig 3.3 (A)). The 1.1 mm thick control layer (borofloat glass) includes valve seats where pressurized air and vacuum are connected to close and open, respectively. The 500 µm thick flow layer (0211 glass) includes microchannels for sample flow and a rectangular hole that serves as a reaction cell. A peristaltic pump is created once the three valves are connected in a row (Fig 3.3 (B)).

Figure 3.4 summarizes the fabrication procedure for the control and flow glass layers in tri-layer fluidic structure. First, 4 inch square glass wafers were hot Piranha-cleaned, sputter-coated with a masking layer of 30 µm of chrome (Cr) and 180 µm of gold (Au) and cold Piranha-cleaned to remove any residual organics on the wafer surfaces. The wafers were subsequently spin-coated with HPR 504 photoresist (Fujifilm) at 500 rpm features were patterned by UV exposure (4 s, 356 nm and with an intensity of 19.2 mW/cm^{-2}) through the chrome mask. Resist development was performed using Microposit 354 developer (Shipley Company) for 25 s while the exposed Cr/Au layer was etched

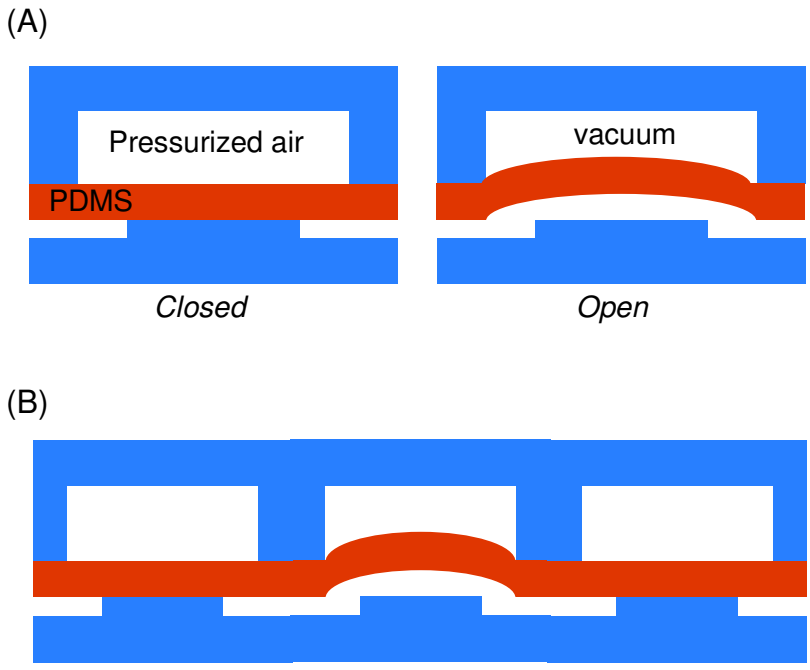

Figure 3.3: Schematics of (A) pneumatic microvalve (B) pneumatic peristaltic micropump

using Cr etch (Arch Chemicals Inc.) and Au etch (0.0985 M I_2 + 0.6024 M KI), respectively. The exposed glass wafers were then isotropically etched in hydrofluidic acid (20 : 14 : 66 HF(49%) : HNO_3 : (70%) : H_2O) to a depth of 90 µm for the control layer and 40 µm for the flow layer. Au and Cr layers were then subsequently stripped off with acetone and the appropriate etchants. Holes for inlet, outlet and air/vacuum access (1 mm in diameter) as well as the resonator cell (3.5 mm x 2 mm) were drilled through the glass wafers using a Waterjet system (Bengal, Flow International Corp.). The wafers were hot Piranha cleaned again and diced into 2.5 cm x 1.2 cm chips. One glass wafer could make 24 chips.

3.1.3. Microchip Assembly

The arrays of nanoresonators on the silicon chip were aligned with the cell in the flow layer and bonded to the unetched side using an UV epoxy (Norland Optical

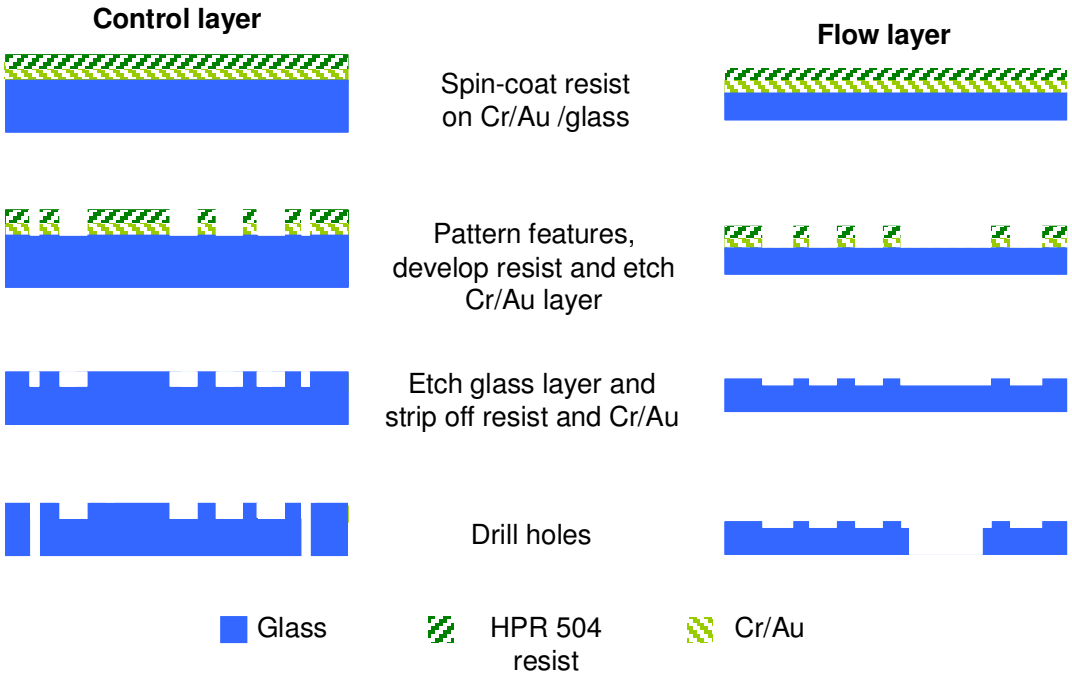

Figure 3.4: Process flow of control and flow layers in tri-layer fluidic architecture

Adhesive 81) (fig 3.5 A). A PDMS membrane (254 µm) and the etched side of the control layer were then irreversibly bonded together using UV exposure [137] (fig 3.5 B). The membrane was subsequently hole punched to create sample access. The PDMS-control layer and the silicon-flow layer were then bonded together to complete the microchip (fig 3.5 C). The glass layers can be recycled by removing the PDMS through pentane submersion and a subsequent Piranha clean [138]. The overall cross section and the top view of the microchip

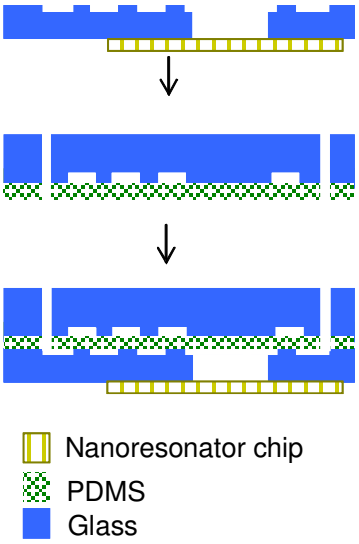

Figure 3.5: Microchip assembly flow

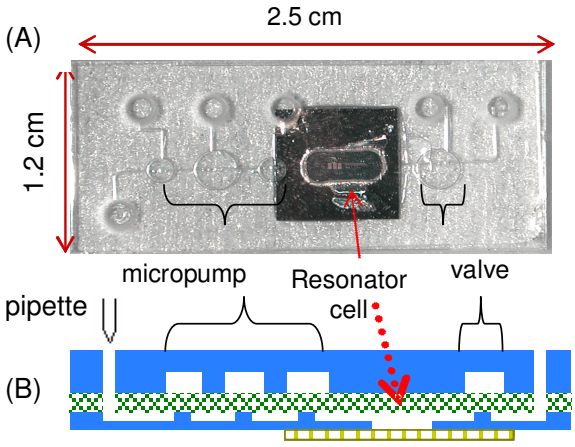

Figure 3.6: Microchip (A) top view (B) cross section

are shown in Figure 3.6.

3.2 Experiment and Result

3.2.1 Fluid Handling

Experiments were conducted to test the automated fluidic handling capabilities of the microchip. The chip was mounted on a platform and connected to in-house air/vacuum sources which were controlled by a custom-built microcontroller-driven circuitry [137] (Fig 3.7). Pressures of – 7.4 psi and 20 psi were used to open and close the microchannel, respectively. Liquid samples such as DI water and ethanol were dispensed from a pipette into the inlet while the pump and the valve were actuated. Approximately 15 s and 18 s were required to fill and purge

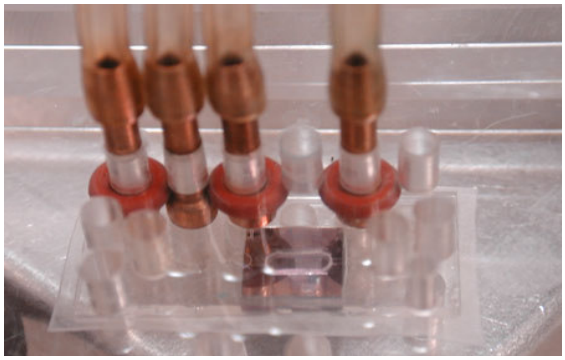

Figure 3.7: Microchip connected to air/vacuum sources on miniaturized pump/valve controlling platform

out the 3.5 µL resonator cell, respectively, using approximately 5.5 µL of liquid. The time and the sample amount required can be reduced by making the resonator cell smaller. The dimensions of the resonator cell (3.5 mm x 2 mm x 500 µm) were chosen such that the alignment of the nanoresonator arrays with the resonator cell could be performed with the naked eyes.

3.2.2 Resonance after Liquid Treatment

Immunoassay commonly involves a series of solution flows for surface modification, antibody-antigen immobilization and the associated washing steps. Therefore, the ability of the encapsulated resonators to resist stiction after flowing liquid was studied by assaying the resonance before and after liquid flow. An interferometry-based resonance-assaying system [139] (Fig 3.8) which has been setup by Dr. Miro Belov from NEMS Lab was used to assay the resonant frequencies of the resonators. The technique relies on the interference of the lights reflected off from the resonator and the substrate. The motion of the resonator changes the height of the gap between itself and the substrate and results in the phase shift of the light traveling through this gap. This produces a small modulation of the reflected signal.

The microchip was mounted on a piezoelectric element inside a small vacuum chamber which was pumped to the 10^{-4} Torr range. The piezoelectric element was actuated by the tracking output of a spectrum analyzer (Agilent model 4411B). A diode laser (λ = 650 nm) beam was directed through a beamsplitter and focused onto the devices with a beam spot of ~ 1.4 µm using a 0.45 numerical aperture microscope objective. The resultant modulated signal was

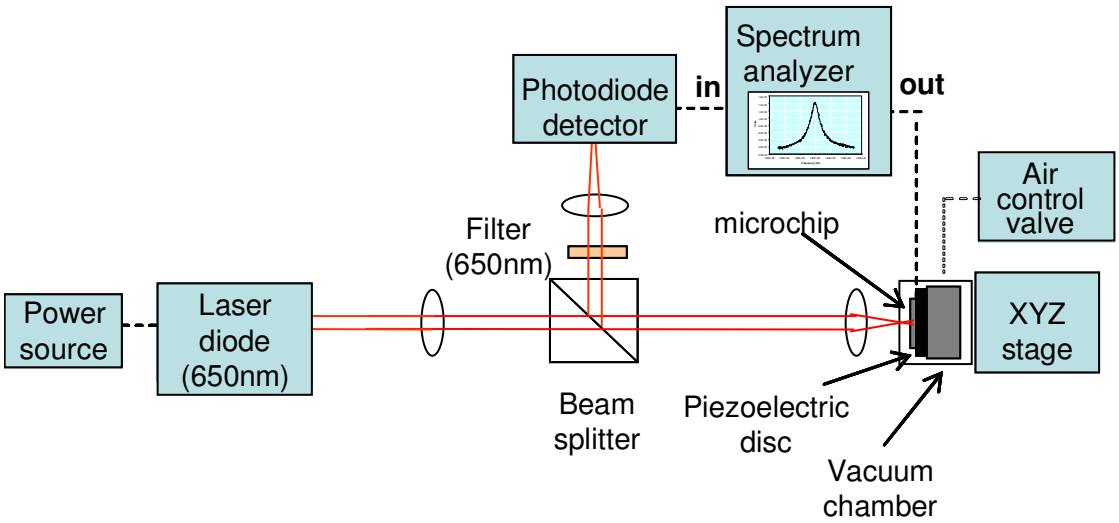

Figure 3.8: Schematic of resonance assaying interferometric system

reflected backward and impinged on an ac coupled photodetector (New Focus model 1601). The photodetector output was then fed to the input of the spectrum analyzer.

Table 3.1 Frequency measurements before and after liquid flow

Measured Resonator Length [Related Measured Frequency, Calculated Frequency]	DI Water		Ethanol	
	Average Δf (kHz)	Average Δf (%)	Average Δf (kHz)	Average Δf (%)
6.8 μm [10MHz, 10.7 MHz]	5.1	0.051 ± 0.012	3	0.03 ± 0.01
9 μm [6 MHz, 6.3 MHz]	3	0.05 ± 0.02	1.9	0.032 ± 0.008
10.5 μm [4.5 MHz, 4.7 MHz]	2.2	0.048 ± 0.017	1.3	0.029 ± 0.012

These devices will ultimately be used to detect the attachment of target biomolecules in fluid solution through monitoring of any resonant frequency shift associated to their mass. However, immersion in fluid solution can by itself modify the surface of the devices and/or contaminate it with other material, possibly inducing frequency shifts that would be unrelated to the attachment of the target of interest. In order to assess this possibility, initial control experiments were performed where freshly fabricated resonators were immersed in deionized water and ethanol. The calculated (Eq. 2.5) and measured resonance frequencies for 6.8 μm, 9 μm and 10.5 μm long cantilevers were 10.7 MHz and 10 MHz, 6.3 MHz and 6 MHz, and 4.7 MHz and 4.5 MHz, respectively. The experimentally measured resonant frequency was systematically lower than the predicted one by 5 to 7 %. This is likely vaused by a small undercut of the anchor point that effectively elongates the resonant structure compared to its design length,

lowering the experimentally-observed resonant frequency. Following the first resonance-assaying, ethanol or DI water was then pumped into and kept in the resonator cell for 30 min. Following purging the cell, each chip was dried with nitrogen and subjected to resonance assaying again in the interferometric setup. Table 3.1 summarizes the frequency shift (Δf) for each beam length averaged over the measurements from more than 12 chips after liquid treatment. The percent frequency shifts averaged over the three beam lengths due to DI water and ethanol exposure were 0.05 ± 0.02 % and 0.03 ± 0.01 % respectively. In addition, this test conclusively demonstrated that the resonators were resistant to stiction following exposure to fluid.

3.3 Conclusion

A microfluidic device was developed with integrated arrays of silicon nanoresonators and automated pneumatic micro pumps and valves. The integrated resonators were 340 nm thick, 700 nm wide and 6.8 μm, 9 μm, and 10.5 μm long, and presented resonant frequencies of 10 MHz, 6 MHz and 4.5 MHz, respectively. The pneumatic micro pump and valves were based on a tri-layer architecture consisting of two glass layers and a PDMS membrane. This device utilized a liquid sample of 5.5 μL to fill a 3.5 μL resonator cell and the automated micropump delivered the sample at ~ 0.23 μL/s. The resonance assaying before and after a liquid flow demonstrated the feasibility of the resonators to work in the microfluidic system. The measured frequency shifts due to the flow of each DI water and ethanol were approximately 0.05 ± 0.02 % and 0.03 ± 0.01 % respectively, and these shifts from the plain liquids put a lower limit on the sensitivity of the devices. The resonators were resistant to stiction and their resonance abilities were retained after liquid treatment in the fluidic system. This is the first time demonstration of integrating NEMS resonators with on-chip and automated sample delivery system on a chip. The encapsulation of the resonator-based sensing platform in the system provided an increased device

portability with being less susceptible to contamination and inter-run variation and a reproducible performance baseline for sensor systems.

Chapter 4
Resonator Performance

4.1. Introduction

Nanomechanical resonators must operate at reduced pressures in order to avoid Q factor degradation due to viscous damping. However, viscous damping is an unavoidable challenge for resonant devices in chemical- or bio- sensing where detection is carried out in air or liquid. The resonator must operate in a non-vacuum environment to realize the concept of lab-on-a-chip at its full potential.

There have been efforts to improve the operation of resonant sensors in air or liquid by: the use of higher order modes as the associated increase in the frequency can significantly increase the intrinsic sensitivity compared to the fundamental bending mode for a given cantilever as illustrated in Eq. 2.4 [3-4, 9-10], and the use of the lateral, in-plane mode or the torsional mode in addition to the higher harmonics as it has also exhibited larger Q factors than the fundamental bending mode [156]. The double paddle resonator in torsional mode

is an example of another device showing improved performance using higher order modes, demonstrating a reduction of internal friction by a several orders of magnitude [10]. Also, Burg *et al.* [151-152] made a significant innovation by encapsulating a microchannel within a resonator instead of the opposite. Viscous damping was thus avoided and the Q factor was unaffected. In addition, the choice of actuation technique has shown to improve the Q factor in a viscous environment [40, 41].

In this chapter, we investigate the impact of the actuation techniques chosen on the Q factor of the nanoresonator encapsulated in a micro-cell. Specifically, photothermal and piezoelectric actuations have been chosen for this comparison. We first compare their theoretically and experimentally obtained Q factors at varying pressure to show that those experimental values are reliable and consistent with the theory. Then, the effect of encapsulating nanoresonators in a micro-cell on the Q factor is investigated. Finally, the effect of the choice of actuation technique on Q factor is investigated by specifically comparing photothermally and piezoelectrically actuated resonators at varying pressure.

4.2. Theoretical and Experimental Q Factors

4.2.1 Theoretical Q Factor Calculation

The overall Q factor is calculated (Eq. 2.8) based on the Q factors associated with thermoelastic damping (TED), support loss and air damping as introduced in Chapter 2. The lowest individual Q factor of the three is the limiting factor to the overall Q factor. A theoretical resonator, 10 μm long, 700 nm wide and 340 nm thick made of single crystal silicon, is used for these calculations. The TED-associated and support loss Q factors are calculated from Eq 2.9 – 2.12 using the values summarized in table 4.1.

The performance of a resonator operating in a non-vacuum environment is strongly influenced by either the surrounding air pressure in molecular regime or the viscosity of surrounding fluid in viscous regime. The specific regime of operation is determined by the Knudsen number, Kn. A resonator operates in viscous region for Kn < 0.01 and in

Table 4.1. Values of parameters used for the calculation of TED associated Q factor for the standard silicon resonator

Parameter	Parameter Name	Value
T	Absolute temperature	300 K
ρ	Density of silicon	2330 kg/m^3 [60]
f	Fundamental resonant frequency	4.8 MHz
E	Young's modulus	1.70 x 10^{11} N/m^2 [140]
C_P	Specific heat capacity	705 J/(kg-K) [141]
κ	Thermal conductivity	148 W/(mK) [141]
α	Thermal expansion coefficient	2.3 x 10^{-6} K^{-1} [140]
t	Thickness of resonator beam	340 nm

Table 4.2. Values of parameters used for the calculation of Q_{air} for the standard silicon resonator

Parameter	Parameter Name	Value
T	Absolute temperature	300 K
ρ	Density of silicon	2330 kg/m^3 [60]
f_o	Fundamental resonant frequency	4.8 MHz
M	Molar mass of air	28.694 x 10^{-3} kg/mol
P	Pressure	101325 Pa
T	Thickness of resonator	340 nm
R	Universal gas constant	8.314 J/(mol.K)

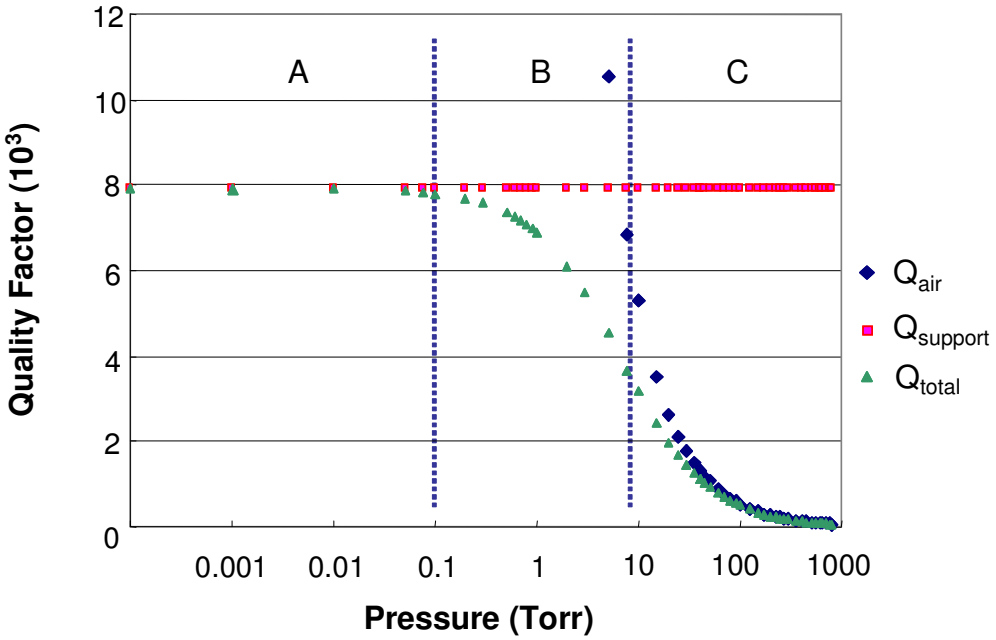

Figure 4.1: Graph of theoretical Q factor at various pressure levels

molecular region for Kn > 10. Using the commonly reported value of $\lambda_{mfp} = 65$ nm [153] in air at atmospheric pressure and setting the size of the beam $w = t$ =340 nm, the Kn for the sample resonator is calculated to be

$$Kn = \frac{\lambda_{mfp}}{w} = 0.2\ [unitless] \qquad (4.1)$$

Therefore, the sample resonator operating at atmospheric pressure falls in the crossover regime. We will however estimate the Q_{air} at high pressure assuming the air damping in molecular regime because no analytical solution exists in the crossover region. Table 4.2 summarizes the values of the parameters in the equations. In Figure 4.1, $Q_{support}$ (square), Q_{air} (diamond) and Q_{total} (triangle) at varying pressure are plotted on the same grid. The Q_{TED} is not shown in the plot since it is in the range of 10^5 at all pressure level. The effect of thermoelastic dissipation is negligible compared to other two loss mechanisms. The Q_{air} below 5 Torr is greater than 10^4 and not shown as well. Also, Q_{air} has mathematically little effect on Q_{total} at P < 0.01 Torr.

From Figure 4.1, we see that $Q_{support} << Q_{air}$ at low pressure and Q_{total} is therefore limited by the support loss (region A). A significant degradation of Q_{total} does not start until the pressure reaches 1Torr (region B) and the rate of degradation starts slowing down from approximately 10 Torr at which the $Q_{support}$ is much higher than Q_{air}. Here, the air damping is the dominant source of loss (region C).

4.2.2 Q Factor Comparison

The Q factor of a 5MHz bare resonator was empirically obtained and compared to the theoretical Q factor at varying pressures to verify the reliability of the setup. The necessary pressures were created through a control valve attached to the vacuum chamber. The valve was slowly opened after the initial pump down to allow air into the chamber. Figure 4.2 shows the curves of experimental (triangle) and theoretical (diamond) Q factors at various pressure points. The trend of the experimental Q factor is clearly consistent with that of the theoretical Q factor. Both experience significant degradation starting at

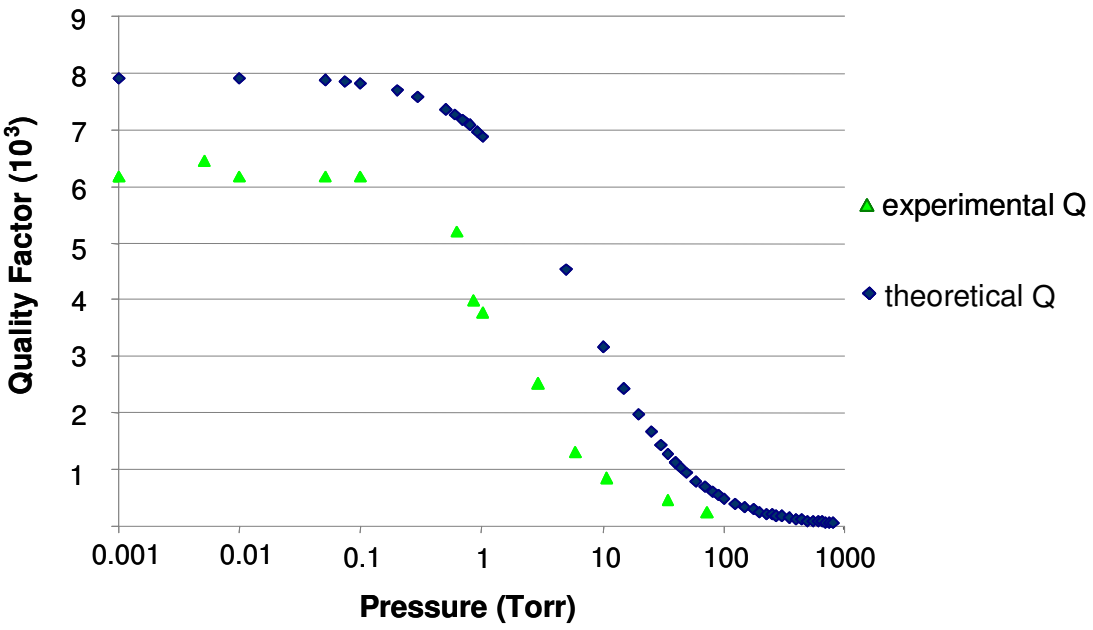

Figure 4.2: Graph of experimental and theoretical obtained Q factors at varying pressure

approximately 1 Torr and the degradation slows down at approximately 10 Torr. This trend agrees with results previously reported by Aubin *et al.* [18]. The discrepancy in the values can be explained by the surface loss (2.1.2.4) which becomes a significant effect at low pressure as the surface-to-volume ratio of the resonant device increases [55, 60]. This consistent trend of experimental and theoretical Q factors assures that the currently used measurement setup and the nanoresonator performance are reliable.

4.3. The Effect of Encapsulation on Q Factor

The effect of encapsulating the resonators in the resonator cell on the Q factor was studied by measuring the Q factor of the same resonator before and after the encapsulation. First, a bare resonator chip was installed in the vacuum chamber and the Q factor was measured while the system was leaked at various rates after being pumped down. The resonator was then taken out of the vacuum and encapsulated in a microfluidic cell by assembling the microchip. The chip was

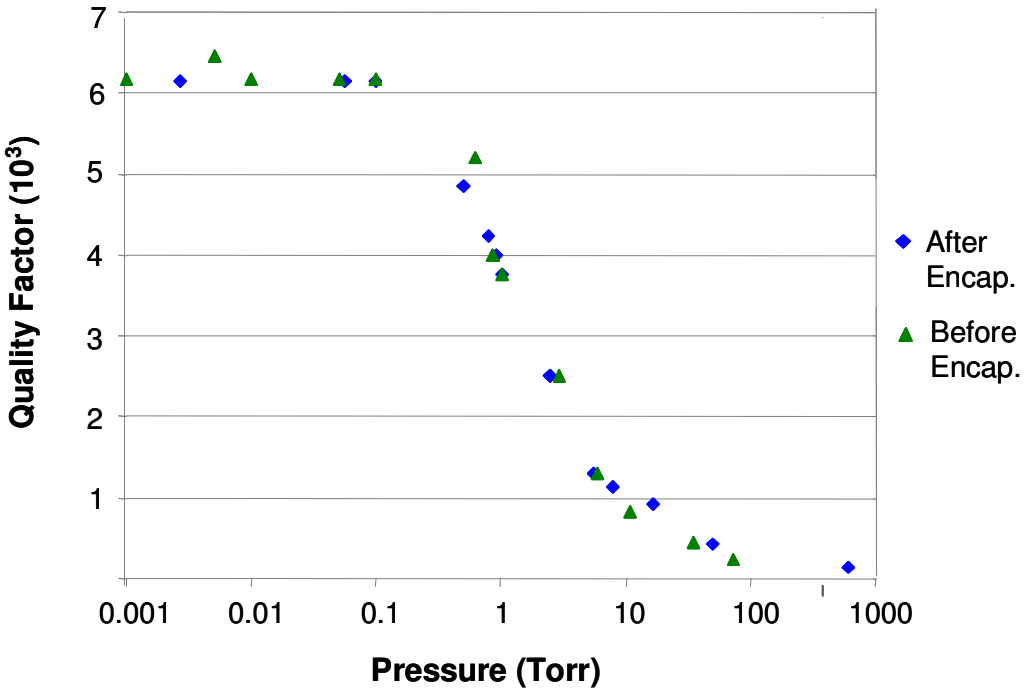

Figure 4.3: Graph of Q factors before and after encapsulation

then re-installed into the vacuum chamber and the Q factor measurements were repeated. Figure 4.3 shows the resultant curves of Q factor at varying pressure before (triangle) and after (diamond) encapsulation. Both curves are in good agreement. Even though the pressure inside the micro cell could not be directly measured after encapsulation, the resulted plot assures that, first, the Q factor reached while pumping down the microfluidic channels/microcell was maximized due to the removal of viscous damping effects and not due to reaching an outgassing limited minimum channel pressure [18]. Secondly, a reproducibility of the plot even at various rates of air leakage into the system assures that the pressure change was from the introduction of the air and not from the outgassing or miscommunication of the micro cell to the external vacuum system. In conclusion, the effects of encapsulation on the resonance performance were negligible.

4.4 The Effect of Actuation Mechanism on Q Factor : Piezoelectric vs. Photothermal

An appropriate choice of actuation mechanism has been reported to improve the performance of resonators in viscous environment by reducing the obscuring signals that can be generated by actuation mechanisms [40, 41]. Among the various actuation mechanisms introduced in Chapter 2, here we focus on photothermal actuation in comparison to the piezoelectric actuation.

Photothermal actuation is an attractive mechanism especially in integration with optical interferometric assaying setup. This mechanism has demonstrated of its capability of working in high pressure environments. Sekaric *et al.* [142] achieved a Q factor greater than 1000 in air at room temperature with an optically-driven paddle-shaped resonator. Sampathkumar *et al.* [143] and Lavrik *et al.* [144] have obtained the Q factor of 30 ~ 54 and femtogram mass detection at ambient pressure. Verbridge *et al.* [145] have reported a Q factor of ~ 400 in

air and ~5 in liquid for an optically driven resonator. Photothermal actuation scheme integrated with an optical detection system is advantageous due to absence of external electric or magnetic fields, operation over a wide range of temperature and simple fabrication process of resonators [142, 145].

Figure 4.4 shows the schematic of the photothermal actuation system, set by Dr. Miro Belov in NEMS Lab, in the existing interferometry detection setup [79]. Only minor changes were required to switch from the piezoelectric actuation (Fig 3.8) to the photothermal actuation while the microchip fabrication process remains unchanged. The newly added components are indicated in italic bold letters. Resonator actuation was achieved by focusing an actuating diode laser (λ = 690 nm) on the device anchor. The laser beam was connected to the output of the spectrum analyzer to directly modulate at the resonance. The expected spot size of the focused laser beam and the laser power on the device are 1.4 µm and 1.5 mW respectively.

The microchip was mounted on the piezoelectric disc in the vacuum chamber for comparison of the efficiencies of the two actuation schemes in a wide range of

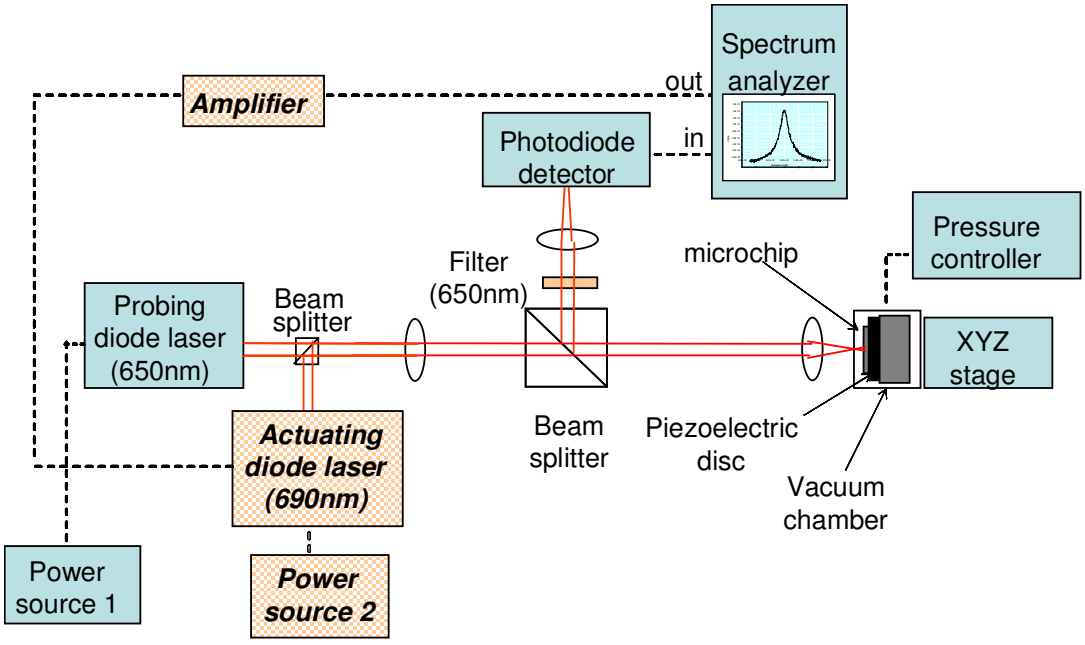

Figure 4.4: The schematic of all-optical actuation and detection setup

pressures. The chamber was initially pumped down to ~ 10^{-4} Torr and the pressure -control valve was then slowly opened to leak the air into the chamber. The resonance response curve from each actuation mechanism was taken on the same resonator at each pressure point by connecting the output port of the spectrum analyzer once to piezoelectric disc and once to the actuating laser source.

Figure 4.5 shows the resonance response curves from each actuation at pressures of 1, 75 and 750 Torr. The piezoelectrically driven resonance curve shows distortion and the Q factor becomes undeterminable as pressure increases. The sweep time of the amplitude vs. frequency signal was varied from 0.5 ms down to 0.1 μs over the span of 30 kHz to 400 kHz to ensure that the distortion is real and not an overlap of the current and the previously scanned signals. This

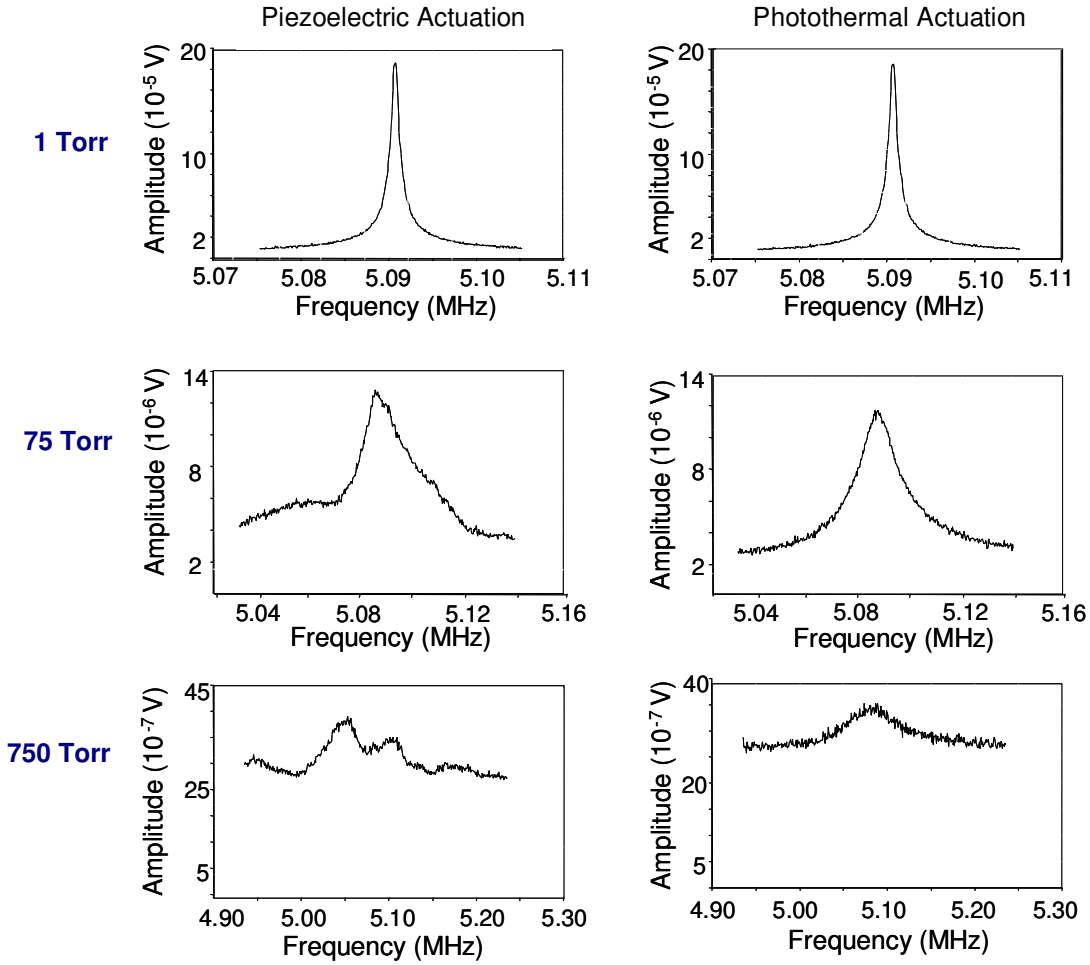

Figure 4.5: Resonance response curves of photothermal and piezoelectric actuations

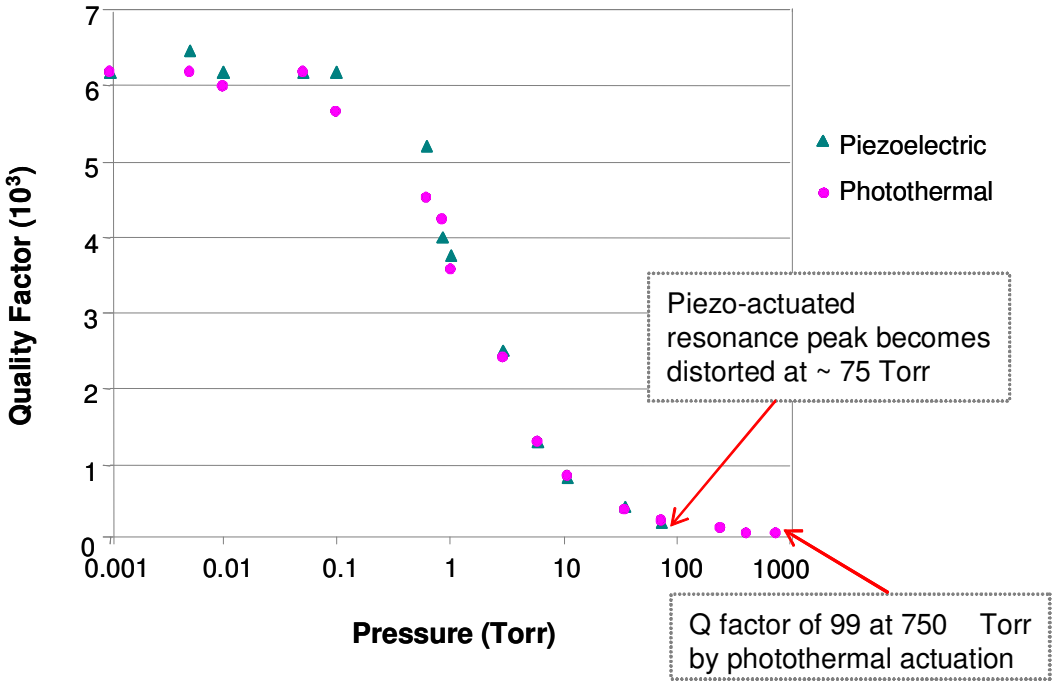

Figure 4.6: Graph of Q factors of piezoelectrically and photothermally actuated resonators

distortion remained the same even at different scanning intervals. This implies that the distortion is real with respect to having the signal being reproduced during each scan. On the other hand, the response curve of the photothermally driven resonator maintained the Lorentzian curve shape and the Q factor of ~ 100 was achieved even at atmospheric pressure (Fig 4.7). The superior performance of photothermally actuated devices to that of piezoelectrically actuated ones has been previously reported [145]. The lower efficiency of piezoelectric actuation in air is attributed to the background signals including the resonances from air molecules that can obscure the small resonance signals from the resonators. Photothermal actuation provides a non-contact and point-like method for resonator excitation in air [143] and thus allows easy identification of the resonance without the presence of spurious data. This result provides the promising potential use of the developed microfluidic chip in more practical biosensing applications with increased portability through the elimination of the expensive vacuum system and the improvement of integrating the optical components into a compact system.

4.5 Conclusion

The performance of the resonators has been studied using Q factors. First, the trend of experimental Q factors showed consistency with theory. This assures that our experimental setup and the measured data are reliable. Second, the investigation on the effect of resonator encapsulation in the resonator cell of which volume is in millilitre range showed that the encapsulation has little effect on the performance of the device. Lastly, the effect of choice of actuation mechanism on the Q factor was studied by comparing Q factors of piezoelectric- and photothermally- driven resonators. Photothermal actuation was found as a better choice than piezoelectric actuation for resonators operated in ambient atmosphere. This result provides the feasibility of the use of the developed microfluidic chip in more practical bioassaying applications with increased portability through the elimination of the expensive vacuum system.

Chapter 5
Protein Detection

Chapter 2 presented a review on MEMS/NEMS devices and their applications in chemical and biological analysis. We described in Chapter 3 the design and fabrication of nanoresonator-based microfluidic chips, and demonstrated the automated on-chip fluid handling as well as the feasibility of the resonators to work in the system. We also showed in Chapter 4 that the device performance is in accordance with the theory at a wide range of pressure levels. In addition, the all-optical transduction technique has been shown to perform better at ambient pressure. This chapter combines all of the previous work together and demonstrates the biosensing proof-of-concept of the integrated microfluidic device. The biotin-streptavidin complex has been chosen to test the biosensing capabilities of the devices since it is readily available and well-understood.

5.1 Surface Modification

5.1.1 Introduction

Detection of specific biological analytes requires functionalization of the sensing surface with the corresponding specific receptors. Immobilization of the receptors on the surface can typically be achieved using self-assembled monolayers.

Self-assembled-monolayers (SAMs) are long-chain organic molecules that spontaneously self-organize onto the surfaces of appropriate substrates to form stable, well-defined structures [146]. A generic SAM molecule consists of a surface-active head group that attaches to its corresponding substrate surface, an alkyl or derivatized alkyl group (C_xH_y) which through van der Waals interactions

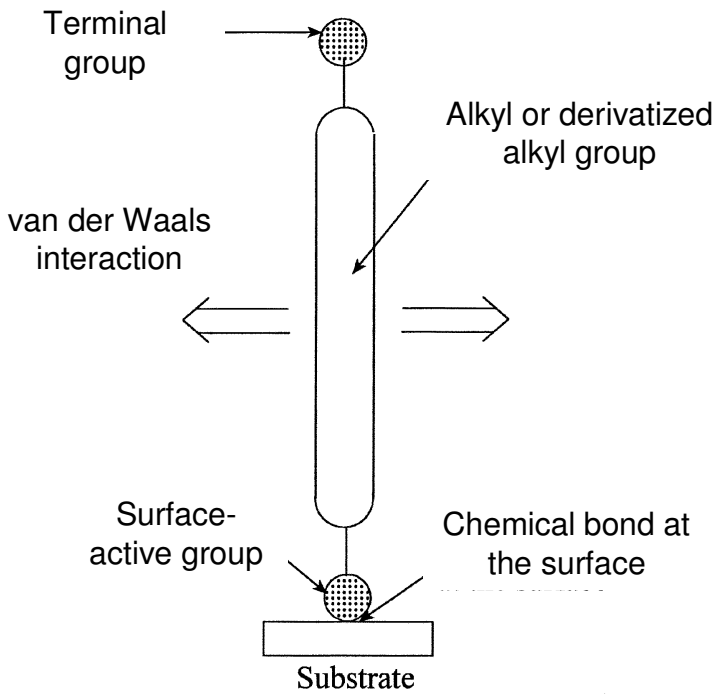

Figure 5.1: Schematic of a self-assembled monolayer on a surface

assists in densely packed self-organization, and a highly-customizable terminal group to which other species can bind [2] (Fig 5.1). SAMs are usually produced by immersing a substrate in the solution containing precursor (ligand) that is reactive to the substrate surface, or by exposing the substrate to the vapour of the reactive chemical species [147]. The two common SAMs used for immobilization of biomolecules are alkane-thiols and organo-silanes. Alkanethiolated SAMs have a S-H head group in which the sulphur has strong and stable affinity to gold surface, and have been widely used as a biosensing platform. Organosilane SAMs have a silane as the surface-active head group and are created by attachment of the head group to the hydroxylated silica (Si-OH) substrate forming siloxane bonds (Si-O-Si) [2]. Although alkanethiolates have been the most frequently used SAMs in surface biofunctionalization, the requirement of gold-coated surfaces can decrease the Q factor and complicate the fabrication process when used in nanoscale resonators [148].

The following section describes the vapour-based surface modification of the silicon nanoresonators with organosilane SAMs. Mercaptopropyl trimethoxysilane (MPTMS) is employed as the SAM on the resonators for the subsequent immobilization of the biotin-streptavidin complex.

5.1.2 Experiment

Arrays of nanoresonators integrated with microfluidic systems have been fabricated along the design and procedure described in Chapter 3. The resonator chip was bonded to a flow glass layer and subjected to a first-time resonant frequency measurement prior to surface modification. The bonded chip was then covered with a piece of PDMS such that only the silicon resonator chip is modified with the reactive chemical species while the rest of the surface of the glass layer is protected from the silanization.

A set of two bonded chips, chip A and chip B, were oxygen cleaned for 90 s to ensure the presence of silanol groups for silanization. Only chip A was placed inside a vacuum desiccator with an open vial containing 100 μL of MPTMS (95% pure, Sigma-Aldrich). The chamber was then pumped down to 200 mTorr and left sealed for 16 hours. The chip was then rinsed with ethanol to remove the unbound MPTMS molecules and the PDMS masking layers were removed from both chip A and chip B. Each chip was then fully assembled by bonding to the layers of PDMS-control glass and subjected to resonance assaying in vacuum for a second time.

5.1.3 Result

The resonators in chip A were O_2 cleaned and underwent silanization whereas chip B was O_2 cleaned only. Each process step has an associated mass added to the resonators. The frequency shifts measured from both chips were then compared to calculate the shift due to the deposition of the MPTMS layers only. Table 5.1 summarizes the measured and calculated average shifts of the resonators on both chips as well as the detected mass-per-area of each beam length. The mass-per-area averaged from the three beam lengths is 2.32 $\pm$ 0.03 mg/m^2. Since MPTMS is trifunctional, it allows the molecules to bond to the surface as well as to bond laterally with each other to form a multilayer [152]. Therefore, using a MPTMS molecular mass of 196.34 g/mol (Sigma-Aldrich), this corresponds to 7.1 x 10^{18} MPTMS molecules per m^2 and 7.1 MTPMS monolayers assuming each MPTMS molecule occupies ~ 1 (nm)^2 [152].

Table 5.1: Summary of frequency shifts and corresponding mass-per-area calculation

Resonator Length [Related Frequency]	Chip A <O_2 Clean & Silanization>	Chip B <O_2 Clean Only>	Silanization	
	Average Δf (kHz)	Average Δf (kHz)	Average Δf (kHz)	Mass/Area (mg/m^2)
7 µm [10.05MHz]	110	65	45	2.32
9 µm [5.96 MHz]	65	38	27	2.36
10 µm [4.76 MHz]	53	31	21	2.3

5.2 Protein detection

The applicability of this integrated microfluidic device to biomolecular detection was demonstrated using streptavidin as target protein, an biotin as itsspecific probe. The biotin-streptavidin complex was chosen as test system given its very high affinity and stability [21].

In order to attach streptavidin onto the resonator surface, first, the thiol (-SH)-terminated MPTMS layers are deposited on the Si surface (Fig 5.2 (1)). The surface is then treated with thiolated-biotin (Biotin-HPDP, Pierce Biotechnology) which readily forms a covalent disulfide bond (S-S) with the thiol group on the MPTMS layer (Fig 5.2 (2)). Finally, streptavidin with four biotin-binding sites

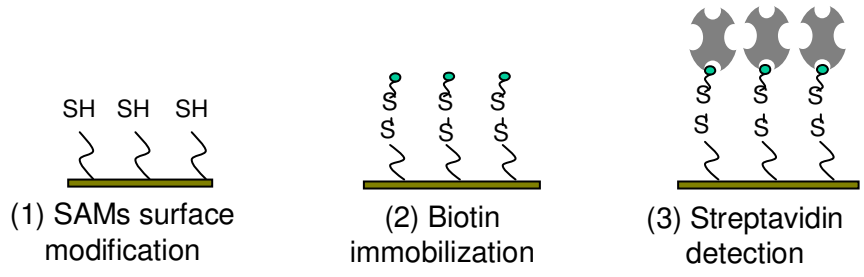

Figure 5.2. Overall process on resonator surface for streptavidin protein detection

(Pierce Biotechnology) is attached to the biotin-functionalized surface (Fig 5.2 (3)).

5.2.1 Experiment

Silicon resonator chips and the glass layers have been fabricated along the design and procedure described in Chapter 3. The resonator chip was then aligned with and bonded to a flow glass layer prior to surface modification.

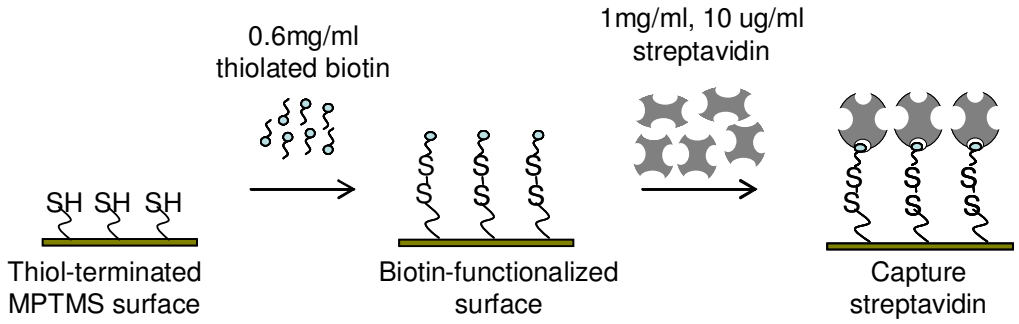

Figure 5. 3: Schematic of resonator surfaces of chip C & D : silanization-biotin-streptavidin

A set of two bonded chips, chip C and chip D, were oxygen cleaned and silanized as described in 5.1, and bonded to the layers of PDMS – control glass. These chips were to be subsequently treated with the solutions containing biotin and streptavidin molecules to investigate the capability of the nanoresonators to distinguishably respond to different molelcules and different concentrations of a given analyte. Each chip was subjected to the resonance assaying. Biotin immobilization was then carried out by dispensing 5.5 μL of 0.6 mg/mL biotin solution into the inlet of the each chip. The biotin solution was made by mixing 1.2 mg/mL of biotin-HPDP in dimethyl sulfoxide (DMSO) with phosphate buffered solution (PBS, 20mM, pH 7.4) using a 1:1 ratio. The solution was delivered to the resonator cell by actuating the integrated pump and valve and

pumped out after a 30 min incubation period. The device rinse was performed by flowing DMSO, DI water and ethanol three times each to the cell to remove unbound biotin molecules from the resonator surfaces. Each chip was then dried with nitrogen [149]. Following a second resonance assaying of each chip, the biotin-functionalized chip C and chip D were treated with 1 mg/mL and 10 μg/mL of streptavidin solutions, respectively. The solutions were made by dissolving streptavidin molecules in PBS (20mM, 0.1% Triton X-100). The solution was pumped out after a 30 min incubation time, and the resonators were rinsed by flowing DI water and ethanol, and dried with nitrogen. Lastly, each chip was subjected to frequency measurement a third time. Figure 5.3 illustrates the process performed to capture streptavidin on the resonator surface in chip C and chip D.

5.2.2 Result

The plot in Figure 5.4 is the result of the measured frequency shifts averaged over three sets of chip C and D run consecutively at different times. The lower concentration of streptavidin solution resulted in smaller frequency shifts as expected since there are less streptavidin molecules available to be captured in the solution. Table 5.2 summarizes the re-evaluated frequency shifts and calculated detected masses of streptavidin averaged across five sets of chips measured at different times. The systematic shift that had been observed following exposure to plain DI (c.f. section (section 3.2.2.) was used as baseline and thus substracted from the raw data. The measured frequency shifts are then used to calculate the mass adsorbed to the resonators using Eq. 2.4. Using molecular weights of 540 g/mol for biotin and 60,000 g/mol for streptavidin (Pierce Biotechnology), the masses of a biotin molecule and a streptavidin molecule are estimated to be 0.89 zg and 99.6 zg, respectively. Given that each streptavidin molecule occupies an area of 45 nm^2 [155], we estimate that the captured streptavidin occupied 81 % of the resonator surface following exposure to the 1 mg/mL solution, and 63 % of the surface following exposure to the 10

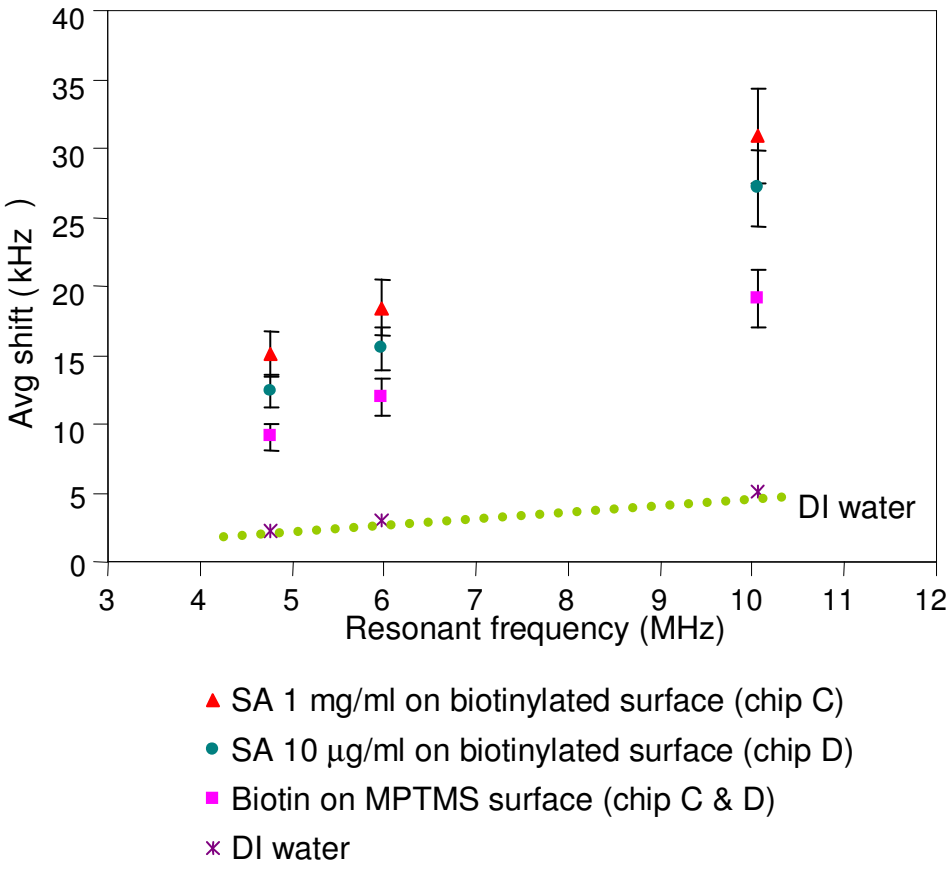

Figure 5.4: Plot of measured frequency shifts due to the specific capture of streptavidin: the dotted line represents the systematic shift observed following exposure to DI water (Section 3.2.2). This shift was used as a base line and substracted from the raw data (chip C and D).

µg/mL solution.

The minimum detectable mass from the resonator arrays is estimated to be 8.83 fg of biotin from the resonator operating at 10 MHz. This was obtained first by subtracting the systematic shift from the measured shift and multiplying with the ratio of the resonator mass to the original resonant frequency (Eq. 2.4).

5.3 Conclusion

A nanoresonator-based integrated microfluidic device was successfully used for the specific detection of the biotin-streptavidin binding complex. The sensing platform for streptavidin detection was created by first modifying the resonator surfaces with thiol-terminated MPTMS monolayers followed by immobilization of thiolated biotin molecules. Streptavidin solutions of 1 mg/mL and 10 μg/mL were then delivered onto the functionalized surfaces. The resonance frequencies were measured in vacuum before and after introducing each sample solution to the resonators. The systematic shift that had been observed following exposure to plain DI water was used as baseline and thus substracted from the raw data. The re-evaluated shifts due to streptavidin on biotin-functionalized surfaces resulted in approximately a mass-per-area of 1.23 mg/m^2 for 1 mg/mL streptavidin solution and a 1.01 mg/m^2 for 10 μg/mL streptavidin solution. These correspond to 80 $(nm)^2$ and 95 $(nm)^2$ occupancy per streptavidin and 81 % and 63 % coverage over the biotin-covered surface, respectively. Also, the current minimum detected mass from the resonators is estimated to be 8.83 fg from the 7 μm long, 340 nm thick and 700 nm wide resonators operating at 10 MHz. This mass sensitivity is comparable to the recently reported cantilever-based detection of biological masses (10^{-12} – 10^{-18} g) [13] using conventional dip-and-dry method.

Although there have been a few demonstration of integrating NEMS resonators into microfluidic systems for biosensing, to the best of our knowledge, this is the first integration with the automated on-chip sample delivery system. Such integration demonstrated a reproducible mass sensitivity comparable to that of the conventional dip-and-dry method while using only a few microliters of sample. The integration with the automated sample delivery systems also yields greater susceptibility to device contamination and inter-run variation, providing less human interruption and accurate control over each flow process involved in the test.

The current system in overall is not fully automated and still bulky involving the external air-vacuum system for the automated sample delivery and a table-size optical system for resonance-assaying. However, a further automation and miniaturization of the systems ultimately into, for example, a hand held device can produce portable, reliable and point-of-care biosensors with an ease of access and use.

Table 5.2 : Summary of re-evaluated frequency shifts and calculated masses of biotin and streptavidin after subtracting the systematic shift

Resonator Length [Frequency]	0.6 mg/mL Biotin (chip C & D)				1 mg/mL Streptavidin (chip C)				10 ug/mL Streptavidin (chip D)			
	Average Δf (kHz)	$\frac{\Delta m}{\Delta f} = \frac{2m_{res}}{f_0}$ (ag/Hz)	Δm (fg)	Mass per Area (mg/m^2)	Average Δf (kHz)	$\frac{\Delta m}{\Delta f} = \frac{2m_{res}}{f_0}$ (ag/Hz)	Δm (fg)	Mass per Area (mg/m^2)	Average Δf (kHz)	$\frac{\Delta m}{\Delta f} = \frac{2m_{res}}{f_0}$ (ag/Hz)	Δm (fg)	Mass per Area (mg/m^2)
7 µm [10.05MHz]	12.1 ± 4.0	0.73	**8.83** ± 2.93	0.62 ± 0.21	23.9 ± 7.0	0.74	17.7 ± 5.2	1.25 ± 0.37	20.0 ± 6.0	0.74	14.8 ± 4.5	1.04 ± 0.31
9 µm [5.96 MHz]	7.74 ± 3.0	1.61	12.4 ± 4.83	0.67 ± 0.26	14.3 ± 3.6	1.61	23.0 ± 5.8	1.24 ± 0.31	11.3 ± 4.2	1.61	18.2 ± 6.7	0.98 ± 0.35
10 µm [4.76 MHz]	5.71 ± 1.92	2.25	12.8 ± 4.32	0.62 ± 0.21	11.8 ± 3.8	2.27	26.8 ± 8.7	1.22 ± 0.42	9.02 ± 2.88	2.27	20.5 ± 6.5	1.00 ± 0.32

.

Chapter 6
Conclusion

6.1. Summary

We developed a microfluidic device that encapsulates silicon nanoresonators as label-free sensing platform. The nanoresonators consist of 6 x 3 arrays at each 6.8 μm, 9 μm and 10.5 μm operating at 4.8 MHz, 6 MHz and 10 MHz, respectively. The microfluidic device includes an integrated pneumatic micro pump and valve for automated sample handling. The device utilizes a liquid sample of 5.5 μL and fills the 3.5 μL cell in 15 s. Resonance assaying before and after treating the resonators with DI water and ethanol showed that the resonators are resistant to stiction after liquid flows and resulted in approximately 0.05% and 0.03% shift respectively. The performance of nanoresonators based on Q factor measurements was investigated at various pressures. The study showed that the experimental and theoretical Q factors are consistent at varying pressure, and the encapsulation of the resonator in a microcell had little effect on the performance. Also, photothermally actuated resonators have shown to perform better

than piezoelectrically actuated resonators at high pressure. The microchip was also tested for its specific biosensing ability. The systematic shift that had been observed following exposure to plain DI water was used as baseline. Two sets of chips were silanized with MPTMS and treated with biotin solution at 0.6 mg/mL. One of the sets was then treated with streptavidin solution at 1mg/mL while the other set was treated with 10 μg/mL. After taking the systematic shift into consideration, the detected mass-per-area of streptavidin was estimated to be 1.23 mg/m^2 for 1 mg/mL and 1.01 mg/mL for 10 μg/mL streptavidin. These correspond to 80 nm^2 and 95 nm^2 occupancy per streptavidin and 81 % and 63 % coverage of the biotin-covered surface, respectively. Also, the minimum detected mass from the resonators was estimated to be 8.8 fg from biotin.

The microfluidic devices with integrated nanoresonator as sensors and on-chip automated pump and valve for fluid handling were developed and successfully demonstrated specific biosensing capabilities.

6.2 Suggested Future Work

6.2.1 Monolithic Structure

A biosensing device needs to be incubated in a solution containing analytes for a sufficient time that enough target analytes are transported by diffusion to the sensing surface for detection. The incubation time can then be reduced if the time for the analyte diffusion is not required. For reduction of the diffusion time, a simple bilayer structure which includes nanoresonators encapsulated in a microchannel (Fig 6.1) can be employed to continuously flow the new analyte solution at a fixed concentration to rapidly replenish the layer in proximity to the sensing surfaces. Figure 6.1 demonstrates the feasibility of encapsulating nanoscale resonators within a 50 μm wide channel. Such structure allows fluid handling with a syringe pump and the reduced structure interior volume can reduce the required sample amount. Our current structure can also be used

for this study to facilitate the on-chip fluid handling if the dimension of the resonator cell is modified to create a laminar flow within itself.

6.2.2 Further Emphasis on LOC System

The requirement of an expensive vacuum system to avoid viscous damping can often hinder the sensitive MEMS/NEMS resonator-based microfluidic devices from more practical applications. We successfully demonstrated in Chapter 4 the capability of our current device for resonance assaying in air using all-optical transduction setup. This foresees the device potentials for biosensing in air with elimination of the vacuum system. In addition, for better sensitivity, a reduction of viscous damping can be achieved by employing inexpensive and portable integrated mini-pump [137] which can be easily pumped down to ~ 200 Torr. The use of such vacuum system to the inlet and outlet of the device can reduce air damping and increase the device portability for its more practical applications.

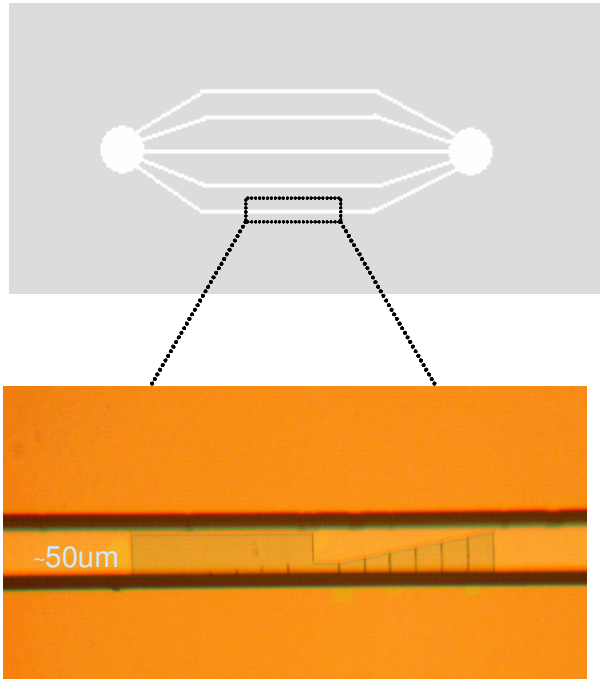

Figure 6.1: Monolithic structure (top) top view of the bilayer chip including 5 channels. (bottom) Each 50 mm wide channel encapsulates an array of nanoresonators.

Finally, parallel detection of multiple analytes can be accomplished by fabricating many individually addressable microfluidic channels with resonator arrays in each and coating the devices with different receptor layers.

References

[1] L. G. Carrascosa, M. Moreno, M. Alvarez, and L. M. Lechuga, "Nanomechanical biosensors: a new sensing tool," *Trac-Trend Anal Chem,* vol. 25, pp. 196-206, 2006.

[2] N. Nashida, W. Satoh, J. Fukuda, and H. Suzuki, "Electrochemical immunoassay on a microfluidic device with sequential injection and flushing functions," *Biosens Bioelectron,* vol. 22, pp. 3167-3173, 2007.

[3] D. Then, A. Vidic, and C. Ziegler, "A highly sensitive self-oscillating cantilever array for the quantitative and qualitative analysis of organic vapor mixtures," *Sensor Actuat B-Chem,* vol. 117, pp. 1-9, Sep 2006.

[4] A. Lopez, C. Mathers, M. Ezzati, D. Jamison and C. Murray, *Global burden of disease and risk factors*, Oxford University Press and the World Bank, New York, NY, 2006.

[5] C. D. Chin, V. Linder, and S. K. Sia, "Lab-on-a-chip devices for global health: Past studies and future opportunities," *Lab Chip,* vol. 7, pp. 41-57, 2007.

[6] P. Yager, T. Edwards, E. Fu, K. Helton, K. Nelson, M. R. Tam, and B. H. Weigl, "Microfluidic diagnostic technologies for global public health," *Nature,* vol. 442, pp. 412-418, 2006.

[7] A. Manz, N. Graber, and H. M. Widmer, "Miniaturized chemical-analysis systems - A novel concept for chemical sensing," *Sensor Actuat B-Chem,* vol. 1, pp. 244-248, 1990.

[8] G. H. W. Sanders and A. Manz, "Chip-based microsystems for genomic and proteomic analysis," *Trac-Trend Anal Chem,* vol. 19, pp. 364-378, 2000.

[9] T. G. Henares, F. Mizutani, and H. Hisamoto, "Current development in microfluidic immunosensing chip," *Analytica Chimica Acta,* vol. 611, pp. 17-30, 2008.

[10] A. Bange, H. B. Halsall, and W. R. Heineman, "Microfluidic immunosensor systems," *Biosens Bioelectron,* vol. 20, pp. 2488-2503, 2005.

[11] T. M. H. Lee and I. M. Hsing, "DNA-based bioanalytical microsystems for handheld device applications," *Analytica Chimica Acta,* vol. 556, pp. 26-37, 2006.

[12] P. S. Dittrich and A. Manz, "Lab-on-a-chip: microfluidics in drug discovery,"

Nat Rev Drug Discov, vol. 5, pp. 210-218, 2006.

[13] P. S. Waggoner and H. G. Craighead, "Micro- and nanomechanical sensors for environmental, chemical, and biological detection," *Lab Chip,* vol. 7, pp. 1238-1255, 2007.

[14] D. Erickson, S. Mandal, A. H. J. Yang and B. Cordovez, "Nanobiosensors: optofluidic, electrical and mechanical approaches to biomolecular detection at the nanoscale," *Microfluid Nanofluid*, vol. 4, pp. 33-52, 2008.

[15] Y. T. Yang, C. Callegari, X. L. Feng, K. L. Ekinci, and M. L. Roukes, "Zeptogram-scale nanomechanical mass sensing," *Nano Lett,* vol. 6, pp. 583-586, 2006.

[16] B. Ilic, D. Czaplewski, M. Zalalutdinov, H. G. Craighead, P. Neuzil, C. Campagnolo, and C. Batt, "Single cell detection with micromechanical oscillators," *J Vac Sci Technolo B,* vol. 19, pp. 2825-2828, 2001.

[17] K. S. Hwang, J. H. Lee, J. Park, D. S. Yoon, J. H. Park, and T. S. Kim, "In-situ quantitative analysis of a prostate-specific antigen (PSA) using a nanomechanical PZT cantilever," *Lab Chip,* vol. 4, pp. 547-552, 2004.

[18] K. L. Aubin, J. Huang, S. M. Park, Y. Yang, M. Kondratovich, H. G. Craighead, and B. R. Ilic, "Microfluidic encapsulated nanoelectromechanical resonators," *J Vac Sci Technolo B,* vol. 25, pp. 1171-1174, 2007.

[19] K. M. Hansen and T. Thundat, "Microcantilever biosensors," *Methods,* vol. 37, pp. 57-64, 2005.

[20] G. G. Stoney, "The tension of metallic films deposited by electrolysis," *Proceedings of the Royal Society of London Series a-Containing Papers of a Mathematical and Physical Character,* vol. 82, pp. 172-175, 1909.

[21] R. Raiteri, M. Grattarola, H. J. Butt, and P. Skladal, "Micromechanical cantilever-based biosensors," *Sensor Actuat B-Chem,* vol. 79, pp. 115-126, 2001.

[22] R. Bashir, J. Z. Hilt, O. Elibol, A. Gupta, and N. A. Peppas, "Micromechanical cantilever as an ultrasensitive pH microsensor," *Appl Phys Lett,* vol. 81, pp. 3091-3093, 2002.

[23] H. F. Ji, K. M. Hansen, Z. Hu, and T. Thundat, "Detection of pH variation using modified microcantilever sensors," *Sensor Actuat B-Chem,* vol. 72, pp. 233-238, 2001.

[24] S. H. Lim, D. Raorane, S. Satyanarayana, and A. Majumdar, "Nano-chemo-mechanical sensor array platform for high-throughput chemical analysis," *Sensor Actuat B-Chem,* vol. 119, pp. 466-474, 2006.

[25] P. Li, X. X. Li, G. M. Zuo, J. Liu, Y. L. Wang, M. Liu, and D. Z. Jin, "Silicon

dioxide microcantilever with piezoresistive element integrated for portable ultraresoluble gaseous detection," *Appl Phys Lett,* vol. 89, 2006.

[26] X. H. Xu, T. G. Thundat, G. M. Brown, and H. F. Ji, "Detection of Hg2+ using microcantilever sensors," *Anal Chem,* vol. 74, pp. 3611-3615, 2002.

[27] H. F. Ji and T. Thundat, "In situ detection of calcium ions with chemically modified microcantilevers," *Biosens Bioelectron,* vol. 17, pp. 337-343, 2002.

[28] H. F. Ji, T. Thundat, R. Dabestani, G. M. Brown, P. F. Britt, and P. V. Bonnesen, "Ultrasensitive detection of CrO42- using a microcantilever sensor," *Anal Chem,* vol. 73, pp. 1572-1576, 2001.

[29] H. F. Ji, E. Finot, R. Dabestani, T. Thundat, G. M. Brown, and P. F. Britt, "A novel self-assembled monolayer (SAM) coated microcantilever for low level caesium detection," *Chem Communs,* pp. 457-458, 2000.

[30] M. K. Baller, H. P. Lang, J. Fritz, C. Gerber, J. K. Gimzewski, U. Drechsler, H. Rothuizen, M. Despont, P. Vettiger, F. M. Battiston, J. P. Ramseyer, P. Fornaro, E. Meyer, and H. J. Guntherodt, "A cantilever array-based artificial nose," *Ultramicroscopy,* vol. 82, pp. 1-9, 2000.

[31] J. Fritz, M. K. Baller, H. P. Lang, H. Rothuizen, P. Vettiger, E. Meyer, H. J. Guntherodt, C. Gerber, and J. K. Gimzewski, "Translating biomolecular recognition into nanomechanics," *Science,* vol. 288, pp. 316-318, 2000.

[32] R. Mukhopadhyay, M. Lorentzen, J. Kjems, and F. Besenbacher, "Nanomechanical sensing of DNA sequences using piezoresistive cantilevers," *Langmuir,* vol. 21, pp. 8400-8408, 2005.

[33] C. A. Savran, S. M. Knudsen, A. D. Ellington, and S. R. Manalis, "Micromechanical detection of proteins using aptamer-based receptor molecules," *Anal Chem,* vol. 76, pp. 3194-3198, 2004.

[34] B. L. Weeks, J. Camarero, A. Noy, A. E. Miller, L. Stanker, and J. J. De Yoreo, "A microcantilever-based pathogen detector," *Scanning,* vol. 25, pp. 297-299, 2003.

[35] B. Dhayal, W. A. Henne, D. D. Doorneweerd, R. G. Reifenberger, and P. S. Low, "Detection of Bacillus subtilis spores using peptide-functionalized cantilever arrays," *J Am Chem Soc,* vol. 128, pp. 3716-3721, 2006.

[36] Y. Arntz, J. D. Seelig, H. P. Lang, J. Zhang, P. Hunziker, J. P. Ramseyer, E. Meyer, M. Hegner, and C. Gerber, "Label-free protein assay based on a nanomechanical cantilever array," *Nanotechnology,* vol. 14, pp. 86-90, 2003.

[37] K. W. Wee, G. Y. Kang, J. Park, J. Y. Kang, D. S. Yoon, J. H. Park, and T. S. Kim,

"Novel electrical detection of label-free disease marker proteins using piezoresistive self-sensing micro-cantilevers," *Biosens Bioelectron,* vol. 20, pp. 1932-1938, 2005.

[38] G. H. Wu, R. H. Datar, K. M. Hansen, T. Thundat, R. J. Cote, and A. Majumdar, "Bioassay of prostate-specific antigen (PSA) using microcantilevers," *Nat Biotechnol,* vol. 19, pp. 856-860, 2001.

[39] C. Ziegler, "Cantilever-based biosensors," *Anal Bioanal Chem*, vol. 379, pp. 946-959, 2004.

[40] S. Timoshenko, D. H. Young, and J. W. Weaver, *Vibration Problems in Engineering,* 4th ed. New York: Wiley, 1974, pp.415-431.

[41] M. D. Ventra, S. Evoy and J. R. Heflim, *Introduction to Nanoscale Science And Technology*, 1st ed. Norwell: KAP, 2004, pp.397, 44-55.

[42] D. Lange, C. Hagleitner, C. Herzog, O. Brand, and H. Baltes, "Electromagnetic actuation and MOS-transistor sensing for CMOS-integrated micromechanical resonators," *Sensor Actuat A-Phys,* vol. 103, pp. 150-155, 2003.

[43] X. M. H. Huang, M. Manolidis, S. C. Jun, and J. Hone, "Nanomechanical hydrogen sensing," *Appl Phys Lett,* vol. 86, 2005.

[44] T. Thundat and L. Maya, "Monitoring chemical and physical changes on sub-nanogram quantities of platinum dioxide," *Surface Science,* vol. 430, pp. L546-L552, 1999.

[45] T. Thundat, E. A. Wachter, S. L. Sharp, and R. J. Warmack, "Detection of mercury-vapor using resonating microcantilevers," *Appl Phys Lett,* vol. 66, pp. 1695-1697, 1995.

[46] B. Rogers, L. Manning, M. Jones, T. Sulchek, K. Murray, B. Beneschott, J. D. Adams, Z. Hu, T. Thundat, H. Cavazos, and S. C. Minne, "Mercury vapor detection with a self-sensing, resonating piezoelectric cantilever," *Rev Sci Instrum,* vol. 74, pp. 4899-4901, 2003.

[47] T. Braun, V. Barwich, M. K. Ghatkesar, A. H. Bredekamp, C. Gerber, M. Hegner, and H. P. Lang, "Micromechanical mass sensors for biomolecular detection in a physiological environment," *Phys Rev E,* vol. 72, p. 9, 2005.

[48] B. Ilic, H. G. Craighead, S. Krylov, W. Senaratne, C. Ober, and P. Neuzil, "Attogram detection using nanoelectromechanical oscillators," *J Appl Phys,* vol. 95, pp. 3694-3703, 2004.

[49] B. Ilic, Y. Yang, K. Aubin, R. Reichenbach, S. Krylov, and H. G. Craighead, "Enumeration of DNA molecules bound to a nanomechanical oscillator," *Nano Lett,* vol. 5, pp. 925-929, 2005.

[50] B. Ilic, Y. Yang, and H. G. Craighead, "Virus detection using nanoelectromechanical devices," *Appl Phys Lett,* vol. 85, pp. 2604-2606, 2004.

[51] J. H. Lee, K. S. Hwang, J. Park, K. H. Yoon, D. S. Yoon, and T. S. Kim, "Immunoassay of prostate-specific antigen (PSA) using resonant frequency shift of piezoelectric nanomechanical microcantilever," *Biosens Bioelectron,* vol. 20, pp. 2157-2162, 2005.

[52] B. Ilic, D. Czaplewski, H. G. Craighead, P. Neuzil, C. Campagnolo, and C. Batt, "Mechanical resonant immunospecific biological detector," *Appl Phys Lett,* vol. 77, pp. 450-452, 2000.

[53] N. Garcia, A. P. Levanyuk, S. A. Minyukov, and V. T. Binh, "Estimations of the characteristics of GHz range nanocantilevers - eigenfrequencies and quality factors," *Surf Sci,* vol. 328, pp. 337-342, 1995.

[54] J. Ginsberg, *Mechanical Structural Vibrations*, New York: John Wiley and Sons, 2001.

[55] L. D. Landau and E. M. Lifshitz, *Theory of Elasticity*, Oxford, U.K.: Pergamon, 1967

[56] R. Lifshitz and M. L. Roukes, "Thermoelastic damping in micro- and nanomechanical systems," *Phys Rev B,* vol. 61, pp. 5600-5609, 2000.

[57] C. Zener, "Internal friction in solids II. General theory of thermoelastic internal friction," *Phys Rev,* vol. 53, pp. 90-99, 1938.

[58] C. Zener, "Internal friction in solids I. Theory of internal friction in reeds," *Phys Rev,* vol. 52, pp. 0230-0235, 1937.

[59] K. Y. Yasumura, T. D. Stowe, E. M. Chow, T. Pfafman, T. W. Kenny, B. C. Stipe, and D. Rugar, "Quality factors in micron- and submicron-thick cantilevers," *J Microelectromech S,* vol. 9, pp. 117-125, 2000.

[60] J. L. Yang, T. Ono, and M. Esashi, "Energy dissipation in submicrometer thick single-crystal silicon cantilevers," *J Microelectromech S,* vol. 11, pp. 775-783, 2002.

[61] S. Evoy, A. Olkhovets, L. Sekaric, J. M. Parpia, H. G. Craighead, and D. W. Carr, "Temperature-dependent internal friction in silicon nanoelectromechanical systems," *Appl Phys Lett,* vol. 77, pp. 2397-2399, 2000.

[62] B. H. Houston, D. M. Photiadis, M. H. Marcus, J. A. Bucaro, X. Liu, and J. F. Vignola, "Thermoelastic loss in microscale oscillators," *Appl Phys Lett,* vol. 80, pp. 1300-1302, 2002.

[63] K. L. Ekinci and M. L. Roukes, "Nanoelectromechanical systems," *Rev Sci Instrum,* vol. 76, p. 12, 2005.

[64] V. T. Srikar and S. D. Senturia, "Thermoelastic damping in fine-grained polysilicon flexural beam resonators," *J Microelectromech S,* vol. 11, pp. 499-504, 2002.

[65] Y. H. Park and K. C. Park, "High-fidelity Modeling of MEMS resonators - Part 1: Anchor loss mechanisms through substrate," *J Microelectromech S,* vol. 13, pp. 238-247, 2004.

[66] H. Hosaka, K. Itao, and S. Kuroda, "Damping characteristics of beam-shaped micro-oscillators," *Sensor Actuat A-Phys,* vol. 49, pp. 87-95, 1995.

[67] W. E. Newell, "Miniaturization of tuning forks," *Science,* vol. 161, pp. 1320-&, 1968.

[68] C. Vancura, I. Dufour, S. M. Heinrich, F. Josse, and A. Hierlemann, "Analysis of resonating microcantilevers operating in a viscous liquid environment," *Sensor Actuat A-Phys,* vol. 141, pp. 43-51, Jan 2008.

[69] F. R. Blom, S. Bouwstra, M. Elwenspoek, and J. H. J. Fluitman, "Dependence of the quality factor of micromachined silicon beam resonators on pressure and geometry," *J Vac Sci Technol B,* vol. 10, pp. 19-26, 1992.

[70] R. B. Bhiladvala and Z. J. Wang, "Effect of fluids on the Q factor and resonance frequency of oscillating micrometer and nanometer scale beams," *Phys Rev E,* vol. 69, 2004.

[71] C. M. Ho and Y. C. Tai, "Micro-electro-mechanical-systems (MEMS) and fluid flows," *Annu Rev Fluid Mech,* vol. 30, pp. 579-612, 1998.

[72] K. M. Goeders, J. S. Colton, and L. A. Bottomley, "Microcantilevers: Sensing chemical interactions via mechanical motion," *Chem Rev,* vol. 108, pp. 522-542, 2008.

[73] A. Vidic, D. Then, and C. Ziegler, "A new cantilever system for gas and liquid sensing," *Ultramicroscopy,* vol. 97, pp. 407-416, 2003.

[74] C. Vancura, J. Lichtenberg, A. Hierlemann, and F. Josse, "Characterization of magnetically actuated resonant cantilevers in viscous fluids," *Appl Phys Lett,* vol. 87, 2005.

[75] J. Gaspar, V. Chu and J. P. Conde, "Electrostatic actuation of thin-film microelectromechanical structures," *J Appl Phys*, vol. 93, pp. 10018-10029, 2004.

[76] Y. C. Hu, C. M. Chang and S. C. Huang, "Some design considerations on the electrostatically actuated microstructrues," *Sensor Actuat A-Phys*, vol. 112, pp. 155-161, 2004.

[77] J. W. Yi, W. Y. Shih, R. Mutharasan, and W. H. Shih, "In situ cell detection using

piezoelectric lead zirconate titanate-stainless steel cantilevers," *J Appl Phys,* vol. 93, pp. 619-625, 2003.

[78] B. R. Ilic, S. Krylov, M. Kondratovich, and H. G. Craighead, "Optically actuated nanoelectromechanical oscillators," *IEEE J Sel Top Quant,* vol. 13, pp. 392-399, 2007.

[79] B. Ilic, S. Krylov, K. Aubin, R. Reichenbach, and H. G. Craighead, "Optical excitation of nanoelectromechanical oscillators," *Appl Phys Lett,* vol. 86, p. 3, 2005.

[80] N. V. Lavrik, M. J. Sepaniak, and P. G. Datskos, "Cantilever transducers as a platform for chemical and biological sensors," *Rev Sci Instrum,* vol. 75, pp. 2229-2253, 2004.

[81] M. Calleja, J. Tamayo, M. Nordstrom, and A. Boisen, "Low-noise polymeric nanomechanical biosensors," *Appl Phys Lett,* vol. 88, 2006.

[82] M. Calleja, M. Nordstrom, M. Alvarez, J. Tamayo, L. M. Lechuga, and A. Boisen, "Highly sensitive polymer-based cantilever-sensors for DNA detection," *Ultramicroscopy,* vol. 105, pp. 215-222, 2005.

[83] M. Calleja, J. Tamayo, A. Johansson, P. Rasmussen, L. M. Lechuga, and A. Boisen, "Polymeric cantilever arrays for biosensing applications," *Sens Lett,* vol. 1, pp. 20-24, 2003.

[84] P. Ohlckers, A. Hanneborg, and M. Nese, "Batch processing for micromachined devices," *J Micromech Microeng,* vol. 5, pp. 47-56, 1995.

[85] M. Madou, *Fundamentals of Microfabrication: The Science of Miniaturization*, 2nd ed., Boca Raton, FL: CRC Press, 2002

[86] S. A. Campbell, *The Science and Engineering of Microelectronic Fabrication*, 2nd ed. New York: Oxford Univ Press, 2001.

[87] M. Diaz-Gonzalez, M. B. Gonzalez-Garcia, and A. Costa-Garcia, "Recent advances in electrochemical enzyme immunoassays," *Electroanalysis,* vol. 17, pp. 1901-1918, 2005.

[88] Y. L. Bai, C. G. Koh, M. Boreman, Y. J. Juang, I. C. Tang, L. J. Lee, and S. T. Yang, "Surface modification for enhancing antibody binding on polymer-based microfluidic device for enzyme-linked immunosorbent assay," *Langmuir,* vol. 22, pp. 9458-9467, 2006.

[89] D. Erickson and D. Q. Li, "Integrated microfluidic devices," *Anal Chem Acta,* vol. 507, pp. 11-26, 2004.

[90] S. K. Sia and G. M. Whitesides, "Microfluidic devices fabricated in poly(dimethylsiloxane) for biological studies," *Electrophoresis,* vol. 24, pp.

3563-3576, 2003.

[91] J. C. McDonald and G. M. Whitesides, "Poly(dimethylsiloxane) as a material for fabricating microfluidic devices," *Accounts Chem Res,* vol. 35, pp. 491-499, Jul 2002.

[92] J. E. Butler, L. Ni, R. Nessler, K. S. Joshi, M. Suter, B. Rosenberg, J. Chang, W. R. Brown, and L. A. Cantarero, "The physical and functional-behavior of capture antibodies adsorbed on polystyrene," *J Immunol Methods,* vol. 150, pp. 77-90, 1992.

[93] J. E. Butler, "Solid supports in enzyme-linked immunosorbent assay and other solid-phase immunoassays," *Methods,* vol. 22, pp. 4-23, 2000.

[94] J. Davies, A. C. Dawkes, A. G. Haymes, C. J. Roberts, R. F. Sunderland, M. J. Wilkins, M. C. Davies, S. J. B. Tendler, D. E. Jackson, and J. C. Edwards, "A scanning-tunneling-microscopy comparison of passive antibody adsorption and biotinylated antibody linkage to streptavidin on microtiter wells," *J Immunol Methods,* vol. 167, pp. 263-269, 1994.

[95] R. A. Vijayendran and D. E. Leckband, "A quantitative assessment of heterogeneity for surface-immobilized proteins," *Anal Chem,* vol. 73, pp. 471-480, 2001.

[96] Y. L. Bai, W. C. Huang, and S. T. Yang, "Enzyme-linked Immunosorbent assay of Escherichia coli O157 : H7 in surface enhanced Poly(Methyl methacrylate) microchannels," *Biotechnol Bioeng,* vol. 98, pp. 328-339, 2007.

[97] T. S. Phely-Bobin, R. J. Muisener, J. T. Koberstein, and F. Papadimitrakopoulos, "Preferential self-assembly of surface-modified Si/SiOx nanoparticles on UV/ozone micropatterned poly(dimethylsiloxane) films," *Adv Materials,* vol. 12, pp. 1257, 2000.

[98] M. Ouyang, C. Yuan, R. J. Muisener, A. Boulares, and J. T. Koberstein, "Conversion of some siloxane polymers to silicon oxide by UV/ozone photochemical processes," *Chem Mater,* vol. 12, pp. 1591-1596, 2000.

[99] M. T. Khorasani, H. Mirzadeh, and P. G. Sammes, "Laser surface modification of polymers to improve biocompatibility: HEMA grafted PDMS, in vitro assay - III," *Radiat Phys Chem* vol. 55, pp. 685-689, 1999.

[100] G. D. Sui, J. Y. Wang, C. C. Lee, W. X. Lu, S. P. Lee, J. V. Leyton, A. M. Wu, and H. R. Tseng, "Solution-phase surface modification in intact poly(dimethylsiloxane) microfluidic channels," *Anal Chem,* vol. 78, pp. 5543-5551, 2006.

[101] Y. L. Wang, H. H. Lai, M. Bachman, C. E. Sims, G. P. Li, and N. L. Allbritton,

"Covalent micropatterning of poly(dimethylsiloxane) by photografting through a mask," *Anal Chem,* vol. 77, pp. 7539-7546, 2005.

[102] L. Yu, C. M. Li, Q. Zhou, and J. H. T. Luong, "Poly(vinyl alcohol) functionalized poly(dimethylsiloxane) solid surface for immunoassay," *Bioconjugate Chem,* vol. 18, pp. 281-284, 2007.

[103] K. S. Phillips, Y. Dong, D. Carter, and Q. Cheng, "Stable and fluid ethylphosphocholine membranes in a poly(dimethylsiloxane) microsensor for toxin detection in flooded waters," *Anal Chem,* vol. 77, pp. 2960-2965, 2005.

[104] K. S. Phillips and Q. Cheng, "Microfluidic immunoassay for bacterial toxins with supported phospholipid bilayer membranes on poly(dimethylsiloxane)," *Anal Chem,* vol. 77, pp. 327-334, 2005.

[105] Y. Dong, K. S. Phillips, and Q. Cheng, "Immunosensing of Staphylococcus enterotoxin B (SEB) in milk with PDMS microfluidic systems using reinforced supported bilayer membranes (r-SBMs)," *Lab Chip,* vol. 6, pp. 675-681, 2006.

[106] R. Wang, Y. L. Yang, M. Qin, L. K. Wang, L. Yu, B. Shao, M. Q. Qiao, C. Wang, and X. Z. Feng, "Biocompatible hydrophilic modifications of poly(dimethylsiloxane) using self-assembled hydrophobins," *Chem Mater,* vol. 19, pp. 3227-3231, 2007.

[107] S. R. Quake and A. Scherer, "From micro- to nanofabrication with soft materials," *Science,* vol. 290, pp. 1536-1540, 2000.

[108] M. A. Unger, H. P. Chou, T. Thorsen, A. Scherer, and S. R. Quake, "Monolithic microfabricated valves and pumps by multilayer soft lithography," *Science,* vol. 288, pp. 113-116, 2000.

[109] W. H. Grover, A. M. Skelley, C. N. Liu, E. T. Lagally, and R. A. Mathies, "Monolithic membrane valves and diaphragm pumps for practical large-scale integration into glass microfluidic devices," *Sens Actuat B-Chem,* vol. 89, pp. 315-323, 2003.

[110] K. Hosokawa, M. Omata, K. Sato, and M. Maeda, "Power-free sequential injection for microchip immunoassay toward point-of-care testing," *Lab Chip,* vol. 6, pp. 236-241, 2006.

[111] E. Kim, Y. N. Xia, and G. M. Whitesides, "Micromolding in capillaries: Applications in materials science," *J Am Chem Soc,* vol. 118, pp. 5722-5731, 1996.

[112] E. Kim, Y. N. Xia, and G. M. Whitesides, "Polymer microstructures formed by molding in capillaries," *Nature,* vol. 376, pp. 581-584, 1995.

[113] E. Delamarche, D. Juncker, and H. Schmid, "Microfluidics for processing

surfaces and miniaturizing biological assays," *Adv Mater,* vol. 17, pp. 2911-2933, 2005.

[114] E. Delamarche, A. Bernard, H. Schmid, A. Bietsch, B. Michel, and H. Biebuyck, "Microfluidic networks for chemical patterning of substrate: Design and application to bioassays," *J Am Chem Soc,* vol. 120, pp. 500-508, 1998.

[115] E. Delamarche, A. Bernard, H. Schmid, B. Michel, and H. Biebuyck, "Patterned delivery of immunoglobulins to surfaces using microfluidic networks," *Science,* vol. 276, pp. 779-781, 1997.

[116] I. Caelen, A. Bernard, D. Juncker, B. Michel, H. Heinzelmann, and E. Delamarche, "Formation of gradients of proteins on surfaces with microfluidic networks," *Langmuir,* vol. 16, pp. 9125-9130, 2000.

[117] D. Juncker, H. Schmid, U. Drechsler, H. Wolf, M. Wolf, B. Michel, N. de Rooij, and E. Delamarche, "Autonomous microfluidic capillary system," *Anal Chem,* vol. 74, pp. 6139-6144, 2002.

[118] V. Linder, S. K. Sia, and G. M. Whitesides, "Reagent-loaded cartridges for valveless and automated fluid delivery in microfluidic devices," *Anal Chem,* vol. 77, pp. 64-71, 2005.

[119] G. Q. Hu, Y. L. Gao, P. M. Sherman, and D. Q. Li, "A microfluidic chip for heterogeneous immunoassay using electrokinetical control," *Microfluidics and Nanofluidics,* vol. 1, pp. 346-355, 2005.

[120] Y. L. Gao, F. Y. Lin, G. Q. Hu, P. A. Sherman, and D. Q. Li, "Development of a novel electrokinetically driven microfluidic immunoassay for the detection of Helicobacter pylori," *Anal Chim Acta,* vol. 543, pp. 109-116, 2005.

[121] Y. L. Gao, G. Q. Hu, F. Y. H. Lin, P. M. Sherman, and D. Q. Li, "An electrokinetically-controlled immunoassay for simultaneous detection of multiple microbial antigens," *Biomed Microdevices,* vol. 7, pp. 301-312, 2005.

[122] V. Linder, E. Verpoorte, N. F. de Rooij, H. Sigrist, and W. Thormann, "Application of surface biopassivated disosable poly(dimethylsiloxane)/glass chips to a heterogeneous competitive human serum immunoglobulin G immunoassay with incorporated internal standard," *Electrophoresis,* vol. 23, pp. 740-749, 2002.

[123] V. Linder, E. Verpoorte, W. Thormann, N. F. de Rooij, and M. Sigrist, "Surface biopassivation of replicated poly(dimethylsiloxane) microfluidic channels and application to heterogeneous immunoreaction with on-chip fluorescence detection," *Anal Chem,* vol. 73, pp. 4181-4189, 2001.

[124] A. Dodge, K. Fluri, E. Verpoorte, and N. F. de Rooij, "Electrokinetically driven

microfluidic chips with surface-modified chambers for heterogeneous immunoassays," *Anal Chem,* vol. 73, pp. 3400-3409, 2001.

[125] P. Morier, C. Vollet, P. E. Michel, F. Reymond, and J. S. Rossier, "Gravity-induced convective flow in microfluidic systems: Electrochemical characterization and application to enzyme-linked immunosorbent assay tests," *Electrophoresis,* vol. 25, pp. 3761-3768, 2004.

[126] C. Hempen, L. Glasle-Schwarz, U. Kunz, and U. Karst, "Determination of telmisartan in human blood plasma Part I: Immunoassay development," *Anal Chimica Acta,* vol. 560, pp. 35-40, 2006.

[127] E. Eteshola and D. Leckband, "Development and characterization of an ELISA assay in PDMS microfluidic channels," *Sens Actuat B-Chem,* vol. 72, pp. 129-133, 2001.

[128] K. S. Shin, S. W. Lee, K. C. Han, S. K. Kim, E. K. Yang, J. H. Park, B. K. Ju, J. Y. Kang, and T. S. Kim, "Amplification of fluorescence with packed beads to enhance the sensitivity of miniaturized detection in microfluidic chip," *Biosens Bioelectron,* vol. 22, pp. 2261-2267, 2007.

[129] C. A. Wijayawardhana, H. B. Halsall, and R. Heineman, "Micro volume rotating disk electrode (RDE) amperometric detection for a bead-based immunoassay," *Anal Chimica Acta,* vol. 399, pp. 3-11, 1999.

[130] J. W. Choi, K. W. Oh, J. H. Thomas, W. R. Heineman, H. B. Halsall, J. H. Nevin, A. J. Helmicki, H. T. Henderson, and C. H. Ahn, "An integrated microfluidic biochemical detection system for protein analysis with magnetic bead-based sampling capabilities," *Lab Chip,* vol. 2, pp. 27-30, 2002.

[131] J. Rossier, F. Reymond, and P. E. Michel, "Polymer microfluidic chips for electrochemical and biochemical analyses," *Electrophoresis,* vol. 23, pp. 858-867, 2002.

[132] X. B. Yu, D. K. Xu, and Q. Cheng, "Label-free detection methods for protein microarrays," *Proteomics,* vol. 6, pp. 5493-5503, 2006.

[133] B. B. Haab, "Methods and applications of antibody microarrays in cancer research," *Proteomics,* vol. 3, pp. 2116-2122, 2003.

[134] K. H. Lee, Y. D. Su, S. J. Chen, F. G. Tseng, and G. B. Lee, "Microfluidic systems integrated with two-dimensional surface plasmon resonance phase imaging systems for microarray immunoassay," *Biosens Bioelectron,* vol. 23, pp. 466-472, 2007.

[135] R. Kurita, Y. Yokota, Y. Sato, F. Mizutani, and O. Niwa, "On-chip enzyme immunoassay of a cardiac marker using a microfluidic device combined with a

portable surface plasmon resonance system," *Anal Chem,* vol. 78, pp. 5525-5531, 2006.

[136] M. Michalzik, J. Wendler, J. Rabe, S. Buttgenbach, and U. B. Bilitewski, "Development and application of a miniaturised quartz crystal microbalance (QCM) as immunosensor for bone morphogenetic protein-2," *Sens Actuat B-Chem,* vol. 105, pp. 508-515, 2005.

[137] G. V. Kaigala, V. N. Hoang, and C. J. Backhouse, "Electrically controlled microvalves to integrate microchip polymerase chain reaction and capillary electrophoresis," *Lab Chip,* vol. 8, pp. 1071-1078, 2008.

[138] J. N. Lee, C. Park, and G. M. Whitesides, "Solvent compatibility of poly(dimethylsiloxane)-based microfluidic devices," *Anal Chem,* vol. 75, pp. 6544-6554, 2003.

[139] M. Belov, N. J. Quitoriano, S. Sharma, W. K. Hiebert, T. I. Kamins, and S. Evoy, "Mechanical resonance of clamped silicon nanowires measured by optical interferometry," *J Appl Phys,* vol. 103, 2008.

[140] K. R. Virwani, A. P. Malshe, W. F. Schmidt, and D. K. Sood, "Young's modulus measurements of silicon nanostructures using a scanning probe system: a non-destructive evaluation approach," *Smart Mater Struct,* vol. 12, pp. 1028-1032, 2003.

[141] D. R. Lide, *CRC Handbook of Chemistry and Physics,* 76 ed. Boca Raton, FL: CRC, 1995-1996.

[142] L. Sekaric, M. Zalalutdinov, R. B. Bhiladvala, A. T. Zehnder, J. M. Parpia, and H. G. Craighead, "Operation of nanomechanical resonant structures in air," *Appl Phys Lett,* vol. 81, pp. 2641-2643, 2002.

[143] A. Sampathkumar, T. W. Murray, and K. L. Ekinci, "Photothermal operation of high frequency nanoelectromechanical systems," *Appl Phys Lett,* vol. 88, 2006.

[144] N. V. Lavrik and P. G. Datskos, "Femtogram mass detection using photothermally actuated nanomechanical resonators," *Appl Phys Lett,* vol. 82, pp. 2697-2699, 2003.

[145] S. S. Verbridge, L. M. Bellan, J. M. Parpia, and H. G. Craighead, "Optically driven resonance of nanoscale flexural oscillators in liquid," *Nano Lett,* vol. 6, pp. 2109-2114, 2006.

[146] A. Ulman, "Formation and structure of self-assembled monolayers," *Chem Rev,* vol. 96, pp. 1533-1554, 1996.

[147] A. Ulman, "Thermal-stability of langmuir-blodgett and self-assembled films- A possible scenario for order-disorder transitions," *Adv Mater,* vol. 3, pp. 298-303,

1991.

[148] R. Sandberg, K. Molhave, A. Boisen, and W. Svendsen, "Effect of gold coating on the Q-factor of a resonant cantilever," *J Micromech Microeng,* vol. 15, pp. 2249-2253, 2005.

[149] A. Janshoff, K. P. S. Dancil, C. Steinem, D. P. Greiner, V. S. Y. Lin, C. Gurtner, K. Motesharei, M. J. Sailor, and M. R. Ghadiri, "Macroporous p-type silicon Fabry-Perot layers. Fabrication, characterization, and applications in biosensing," *J Am Chem Soc,* vol. 120, pp. 12108-12116, 1998.

[150] T. P. Burg and S. R. Manalis, "Suspended microchannel resonators for biomolecular detection," *Appl Phys Lett,* vol. 83, pp. 2698-2700, 2003.

[151] T. P. Burg, M. Godin, S. M. Knudsen, W. Shen, G. Carlson, J. S. Foster, K. Babcock and S. R. Manalis, "Weighing of biomolecules, single cells and single nanoparticles in fluid," *Nature,* vol. 446, pp. 1066-1069. 2007.

[152] D. K. Aswal, S. Lenfant, D. Guerin, J. V. Yakhmi and D. Vuillaume, "Fowler-Nordheim tunneling and electrically stressed breakdown of 3-mercaptopropyltimethoxysilane self-assembled monolayers," *Nanotech*, vol. 16, pp. 3064-3068, 2005.

[153] E. Cha, C. S. Chiang, J. Enguero and J. J. K. Lee, "Effect of temperature and altitude on flying height," *IEEE T Magn,* vol. 32, pp.3729-3731, 1996.

[154] Instructions EZ-Link Biotin-HPDP 21341, Pierce, www.piercenet.com

[155] E A. Arakaki, S. Hideshima, T. Nakagawa, D. Niwa, T. Tanaka, T. Matsunaga and T. Osaka, "Detection of biomolecular interaction between biotin and streptavidin on a self-assembled monolayer using magnetic nanoparticles," *Biotech Bioeng,* vol. 88, pp. 543-546, 2004.

[156] L. B. Sharos, A. Raman, S. Crittenden and R. Reifenberger, "Enhanced mass sensing using torsional and lateral resonances in microcantilevers," *Appl Phys Lett,* vol. 84, pp.4638-4640, 2004.